

# Advances in Image Correlation Spectroscopy: Measuring Number Densities, Aggregation States, and Dynamics of Fluorescently labeled Macromolecules in Cells

David L. Kolin · Paul W. Wiseman

Published online: 2 October 2007  
© Humana Press Inc. 2007

**Abstract** A brief historical outline of fluorescence fluctuation correlation techniques is presented, followed by an in-depth review of the theory and development of image correlation techniques, including: image correlation spectroscopy (ICS), temporal ICS (TICS), image cross-correlation spectroscopy (ICCS), spatiotemporal ICS (STICS), k-space ICS (kICS), raster ICS (RICS), and particle ICS (PICS). These techniques can be applied to analyze image series acquired on commercially available laser scanning or total internal reflection fluorescence microscopes, and are used to determine the number density, aggregation state, diffusion coefficient, velocity, and interaction fraction of fluorescently labeled molecules or particles. A comprehensive review of the application of ICS techniques to a number of systems, including cell adhesion, membrane receptor aggregation and dynamics, virus particle fusion, and fluorophore photophysics, is presented.

**Keywords** Image correlation spectroscopy · Fluorescence correlation spectroscopy · Membrane dynamics · Fluorescence microscopy · Membrane receptors

## Introduction

The aggregation state of membrane proteins in living cells can be an important indicator of the underlying biology. For example, cytokines and growth factors are thought to exert their effect on cells by causing a dimerization or oligomerization of membrane receptors, which in turn initiate an intracellular signaling pathway [1, 2]. In addition to the aggregation state of cell-surface receptors, their rate and mode of transport can have a number of underlying biological determinants, including protein tethering or corralling by cytoskeletal elements or lipid rafts [3], binding of receptors to extracellular matrix proteins [4], and the membrane-substrate distance [5]. Clearly, to be able to fully understand and characterize the wide range of biochemical reactions which occur within living cells, there must be techniques available to probe the interactions and dynamics of biological macromolecules in situ. The introduction of green fluorescent protein (GFP) and its variants has revolutionized the field of cell biology by allowing an unprecedented specificity and efficiency of fluorescence labeling and live cell imaging [6]. This work will review a number of image correlation techniques which can measure the number densities, aggregation states, dynamics, and interactions of fluorescently labeled membrane proteins including those tagged with GFP or its variants.

The image correlation methods are imaging analogs of fluorescence correlation spectroscopy (FCS), a fluctuation technique developed over 30 years ago to probe the binding of ethidium bromide to DNA molecules in solution [7]. FCS monitors the spontaneous fluctuations of fluorescence intensity collected from fluorophores in a small, open excitation laser beam volume and records the detected fluctuations in photon counts as a time series. The

---

D. L. Kolin · P. W. Wiseman  
Department of Chemistry, McGill University, Montreal, QC,  
Canada H3A 2K6

P. W. Wiseman (✉)  
Department of Physics, McGill University, Montreal, QC,  
Canada H3A 2T8  
e-mail: Paul.Wiseman@McGill.ca

fluctuations in fluorescence arise from any process which changes the occupation number of fluorophores in the focal volume, such as molecular transport or chemical reactions. The time autocorrelation function of the fluctuation time series contains information regarding the dynamics, number density, and reaction kinetics of the system [8–10]. In a traditional FCS apparatus, the laser beam is kept stationary and the experiment is best suited for measuring molecules free in solution or in the cytoplasm. Scanning FCS (SFCS) was later developed as an extension of FCS, in which the laser beam was scanned in a line or circle across the sample, or the sample was translated under the beam, to obtain fluctuation measurements. It was initially used to measure the molecular weight of DNA in solution [11] and later extended to study the aggregation and number density of slowly moving or immobile fluorescent particles such as cell membrane proteins [12], virus particles [13] and lectins [14]. SFCS was also used to determine the diffusion coefficient of fluorescein-labeled proteins [15], and DNA labeled with ethidium bromide in solution as well as colloidal gold-tagged lipids in a planar bilayer [16].

Image correlation spectroscopy (ICS) was developed as the imaging analog of FCS, in which spatial autocorrelation functions are calculated from images of fluorophores (hence spatial fluorescence fluctuations) acquired on laser scanning microscopes [17]. Unlike single-point FCS, ICS does not require “fast” diffusion of fluorophores, making it amenable to the study of slow membrane receptors, receptor clusters, or even chemically fixed cells. The imaging modality is also advantageous because it acquires a large number of spatial samples (pixels) per frame, and does not require sample translation.

A number of fluorescence fluctuation correlation techniques, such as two-photon SFCS [18] and Fourier imaging correlation spectroscopy [19] have been developed which require custom-built apparatuses. While these techniques are powerful methods to measure molecular transport, this work will focus solely on techniques that have been applied to data acquired on commercial confocal or two-photon laser scanning microscopes (LSMs), or total internal reflection fluorescence microscopes (TIRFMs) used with high sensitivity CCD cameras for area detection.

This review will provide an introduction to the existing range of image correlation techniques, which can unlock a wealth of molecular information hidden in images and image time series of fluorescently labeled living or fixed cells recorded using now fairly standard fluorescence imaging systems (e.g., LSMs). The techniques described in this review all use correlation function analysis to extract a few meaningful parameters from a data set containing a huge amount of raw data (Fig. 1). The first part of this review will summarize the theory of the image correlation spectroscopy family of techniques and give guidelines for

their practical application. The second part of the review will highlight their use in a wide range of biological and chemical applications, with an emphasis on quantifying the aggregation state and dynamics of membrane proteins and membrane-associated proteins.

## Image Correlation Techniques

Most of the techniques described in this review can be expressed as a subset of a generalized spatiotemporal correlation function. We will first present the generalized function, and then show how the techniques are variations of this function. The raw data for image correlation analyses is an image series which is really fluorescence intensity, recorded as a function of space and time,  $i(x, y, t)$ , usually obtained from a confocal or two-photon LSM or evanescent wave imaging (TIRFM). We define a generalized spatiotemporal correlation function as [20]:

$$r_{ab}(\xi, \eta, \tau) = \frac{\langle \delta i_a(x, y, t) \delta i_b(x + \xi, y + \eta, t + \tau) \rangle}{\langle i_a(x, y, t) \rangle_t \langle i_b(x, y, t + \tau) \rangle_{t+\tau}}, \quad (1)$$

where a fluctuation in fluorescence,  $\delta i(x, y, t)$ , is given by:

$$\delta i(x, y, t) = i(x, y, t) - \langle i(x, y, t) \rangle_t, \quad (2)$$

where  $i(x, y, t)$  is the intensity at pixel  $(x, y)$  in the image recorded at time  $t$ , and  $\langle i(x, y, z) \rangle_t$  is the average intensity of that image. The subscripts  $a$  and  $b$  in Eq. 1 refer to two different emission wavelength detection channels. For the case of autocorrelation of single detection channel,  $a = b$  and the subscripts are dropped. We will see that most of the techniques reviewed here are described by simplified versions of Eq. 1 for specified limits.

Every image acquired on a fluorescence microscope is a convolution of the microscope PSF with the point-source emission from the fluorophores due to diffraction [21]. This convolution causes the signal from a point-emitter to be spread over a number of pixels. All of the techniques described in this review exploit the microscope PSF to correlate fluorescence fluctuations over space, time, or both (cf. Eq. 1 and Fig. 1). These approaches are inherently powerful because they reduce a huge number of stochastic fluctuations to a few physically meaningful numbers by spatiotemporal averaging.

The act of correlating fluctuations arising from particles within the microscope PSF also confers some critical limitations on ICS approaches. For example, the use of correlation functions means almost all of the techniques presented here assume the system being studied is stationary (i.e., invariant) in either space or time. However, it is clear that this condition may not be met for all measurements in living cells since cells differ in behavior as a

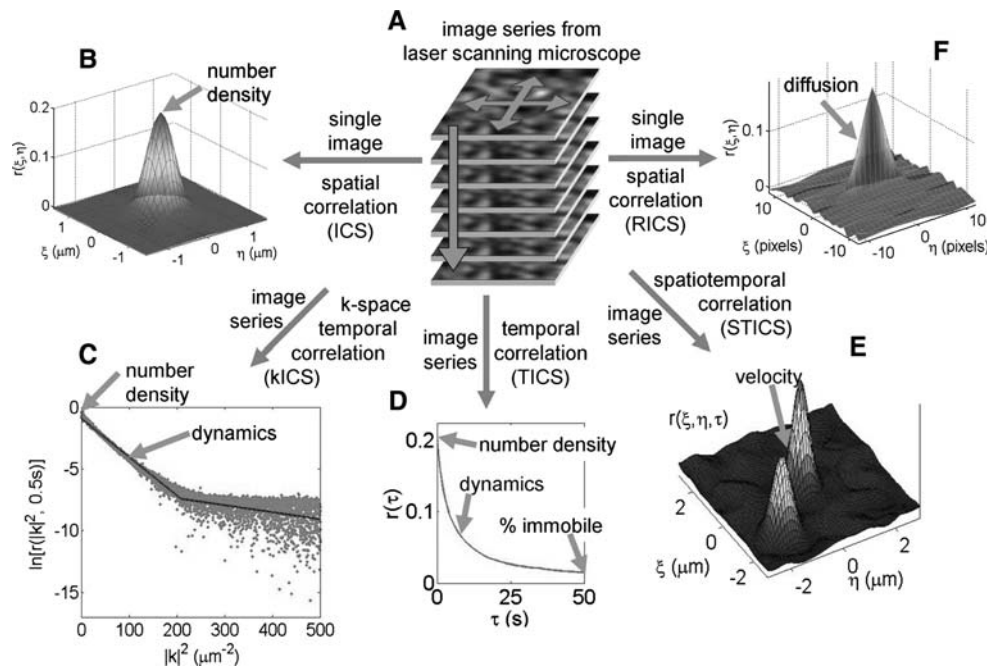


**Fig. 1** An overview of the image correlation techniques described in this review. **(A)** All analyses are performed on an image or image series acquired on a confocal or two-photon laser scanning microscope, or a total internal reflection fluorescence microscope. Frequently, the sample is a cell membrane in which a macromolecule of interest is selectively tagged with a fluorophore, using either antibody labeling or transfection with a fluorescent protein. **(B)** Image correlation spectroscopy (ICS) is performed on an image, and can determine the number density and aggregation state of fluorescently labeled particles. **(C)** k-Space ICS (kICS) measures dynamics (i.e., diffusion and flow) of particles, and is completely insensitive to

fluorophore “blinking” and photobleaching. **(D)** Temporal ICS (TICS) correlates an image series in time to determine dynamics, number densities, and the fraction of the fluorophores that are immobile on the time scale of the measurement. **(E)** Spatiotemporal ICS (STICS) calculates spatial and temporal correlations from an image series to determine the direction and magnitude of flow in the sample. **(F)** Raster ICS (RICS) uses spatial autocorrelation analysis of the fast and slow components of the laser raster scan for an image acquired on a laser scanning microscope to measure fast (e.g., cytosolic) transport dynamics

function of time and are spatially heterogeneous. For example, a membrane-bound protein involved in cell adhesion might exhibit different modes and rates of transport in the front compared to the rear of a migrating cell. The density of this protein may also depend on whether or not it is present in a nascent, mature, or disassembling focal adhesion. Thus, one key assumption in these analyses is that the system studied is at a steady state in the spatial region and over the time period, which is analyzed. Another limitation is introduced by the convolution of the microscope PSF. With the exception of particle ICS (discussed in Section “Particle Image Correlation Spectroscopy (PICS)”), the techniques described here are insensitive to particle movements and interactions below the diffraction limit ( $\sim 200$  nm). For example, temporal ICS cannot resolve the confined diffusion of particles in 50 nm corrals in the cell membrane, and image cross-correlation spectroscopy cannot differentiate between two species which are colocalized in a common 100 nm subcellular compartment and two species that are truly bound to each other. However, techniques such as single particle tracking (SPT) and fluorescence resonance energy

transfer (FRET), respectively, are capable of spatially resolving these processes. Consequently, it is important to understand both the capabilities and limitations of a given method before attempting to study a process of interest.

For non-interacting (i.e., ideal) particles in a noise-free system, in which the measured fluorescence is proportional to the concentration of labeled species, the mean-squared intensity fluctuation divided by the squared mean image intensity is equal to the reciprocal of the mean number of independent fluorescent particles per laser beam volume or area (for two-dimensional (2D) systems such as membranes),  $\langle n_p \rangle$  [8]:

$$\frac{\langle (\delta i)^2 \rangle}{\langle i \rangle^2} = \frac{1}{\langle n_p \rangle}. \quad (3)$$

“Independent particles” refers to separate fluorescent entities, so a linked cluster of monomers would constitute one entity or one independent fluorescent particle. In a real system, the fluctuations (cf. Eq. 2) contain contributions from both signal and noise. In a system without noise,  $\langle (\delta i)^2 \rangle$  could be extracted from the image with a direct

calculation using the pixel intensities. However, in a system with noise, Eq. 3 no longer holds for two reasons. First, noise prevents a direct calculation of the number density because it adds spurious intensity counts to the image, increasing the average intensity. Second, the mean-squared fluctuation term in the numerator of Eq. 3 will also be perturbed, since both noise and signal fluctuations contribute to the recorded intensity fluctuations in an image. The noise in LSM images is usually uncorrelated between neighboring pixels or the same pixel in subsequent images. Such white noise contributions only correlate with themselves within a given pixel and will thus only contribute to the zero-lags value of the correlation function. However, signal measured from real physical sources is correlated in both space and time because of the point spread function (PSF) of the imaging system, which causes single-point emission source to be imaged onto a number of adjacent pixels in an image or at the same pixel location in subsequent images if the source has not moved significantly between images. The spatiotemporal persistence of the signal fluctuations can be exploited to separate them from noise fluctuations, by extrapolating the correlation function to its zero-lags amplitude. For example, in the case of Eq. 1 the autocorrelation function becomes:

$$\lim_{\xi \rightarrow 0, \eta \rightarrow 0, \tau \rightarrow 0} r(\xi, \eta, \tau) = \frac{\langle (i(x, y, t) - \langle i(x, y, t) \rangle_t)^2 \rangle}{\langle i(x, y, t) \rangle_t \langle i(x, y, t) \rangle_t} \quad (4)$$

$$= \frac{\langle (\delta i)^2 \rangle}{\langle i \rangle^2} = \frac{1}{\langle n_p \rangle}.$$

In practice, this value is obtained by fitting the correlation function to an appropriate decay function without weighting the white-noise-containing zero-lags value in the fit. Even with extrapolation to obtain the magnitude of the correlation function,  $\langle i \rangle$  must still be corrected for the signal background [22, 23]. The number of particles or clusters per beam area,  $\langle n_p \rangle$  can be converted to the cluster density (CD), which is the number of particles per  $\mu\text{m}^2$ , by dividing by the area of the laser beam [17]:

$$\text{CD} = \frac{\langle n_p \rangle}{\pi \omega_0^2}, \quad (5)$$

where  $\omega_0$  is the  $e^{-2}$  radius of the focused beam, which is the radius of the microscope PSF. The  $\langle n_p \rangle$  is an indicator of the density of independent fluorescent clusters, but without additional calibration measurements or an estimate of the total number of monomers in the system, it cannot be determined if these particles exist as monomers, dimers, or oligomers. However, the average intensity of the image is

proportional to the total number of fluorophores per beam area assuming quenching does not occur. Therefore, the ratio of  $\langle i \rangle$  and CD provides a measure of the degree of aggregation (DA) [22]:

$$\text{DA} = \frac{\langle i \rangle}{\text{CD}} = c \frac{\langle n_m \rangle}{\langle n_p \rangle} \quad (6)$$

where the factor  $c$  is a proportionality constant, which depends on the spectral characteristics of the fluorophore and the light collection efficiency of the imaging system, and relates the average intensity to the number of monomers. When using antibody labeling, the value of  $c$  can be determined from control measurements of non-specific labeling with the assumption that the non-specifically labeled antibodies are monomers [22]. If the protein of interest is labeled with GFP,  $c$  can be found by imaging a control sample of dispersed GFP monomers under identical conditions as the regular samples [4]. Since the DA is calculated from an image, it can be calculated as a function of time from an image series to measure changes in the aggregation state of a protein [4, 24].

### Image Correlation Spectroscopy

Using the original spatial image correlation spectroscopy (ICS) technique, it is possible to determine the CD and DA from an image of fluorophores acquired on a LSM or TIRFM [17]. As with all of the techniques presented in this review, a correlation function is first calculated from the raw data. This correlation function is then fit to an analytical model to extract the parameters of interest. With spatial ICS, a spatial autocorrelation function is calculated from the intensities recorded in the pixels of individual images.

The normalized intensity fluctuation spatial autocorrelation function of the image recorded at time  $t$  in a time series is given by Eq. 1 when  $\tau = 0$ :

$$r(\xi, \eta, 0)_t = \frac{\langle \delta i(x, y, t) \delta i(x + \xi, y + \eta, t) \rangle}{\langle i(x, y, t) \rangle_t^2}, \quad (7)$$

where the angular brackets denote spatial averaging over the image, and  $\xi$  and  $\eta$  are spatial lag variables corresponding to pixel shifts of the image relative to itself in the  $x$  and  $y$  directions. The original ICS technique was a 2D method, and we have adopted the more encompassing notation here to reflect extensions of the method to the time domain. To minimize computation time, these functions are typically calculated using Fourier methods [17]:



$$r(\xi, \eta, 0)_t = \frac{\mathcal{F}^{-1}[\mathcal{F}(i(x, y, t))\mathcal{F}^*(i(x, y, t))]}{\langle i(x, y, t) \rangle_t^2} - 1 \quad (8)$$

where  $\mathcal{F}$  denotes the 2D spatial Fourier transform,  $\mathcal{F}^*$  is the complex conjugate of this transform, and  $\mathcal{F}^{-1}$  is the inverse 2D spatial Fourier transform. The correlation function is then fit to a 2D Gaussian using a three parameter nonlinear least squares algorithm (fit parameters are in bold):

$$r(\xi, \eta, 0)_t = \mathbf{g}(\mathbf{0}, \mathbf{0}, \mathbf{0})_t \exp\left[-\frac{\xi^2 + \eta^2}{\omega_0^2}\right] + \mathbf{g}_{\text{off}}. \quad (9)$$

where  $\mathbf{g}(\mathbf{0}, \mathbf{0}, \mathbf{0})_t$  is the zero-lags amplitude, and  $\mathbf{g}_{\text{off}}$  is the long-spatial lag offset to account for an incomplete decay of the correlation function. A Gaussian function is used because the laser beam acts as the spatial correlator and has a Gaussian intensity profile.

As described earlier, the zero-lags amplitude of the correlation function is inversely proportional to the number of independent fluorescent particles per beam area,  $\mathbf{g}(\mathbf{0}, \mathbf{0}, \mathbf{0})_t = 1/\langle n_p \rangle$ . Cluster densities can be calculated from  $\langle n_p \rangle$ , using the fit  $\omega_0$  (cf. Eq. 5) [17, 23]. The value of  $\omega_0$  obtained from the fit to Eq. 9 is usually the value used when calculating the CD (cf. Eq. 5), and is a useful indicator of the quality of the fit. If the fitted value of  $\omega_0$  differs by more than 30% from a measured value for the beam radius, the fit should be discarded [17, 25]. The beam radius of the microscope PSF can be determined using a number of methods, including imaging sub-diffraction-limit diameter fluorescent microspheres [26], or using the gold-foil edge technique [17]. Because the size of  $\omega_0$  is wavelength-dependent, the PSF should be measured at the same excitation wavelength as the fluorophore in the ICS experiment. An example ICS measurement, with the raw

correlation function and fitted 2D Gaussian surface, is shown in Fig. 2.

Spatial ICS is usually applied to images acquired on LSMs. However, a variant was successfully used on images from a TIRFM [27]. Unlike a LSM, the evanescent wave used to excite the fluorophores in a TIRFM has a non-uniform Gaussian intensity profile, and this complication must be corrected for in a quantitative analysis [27].

### *Spatial ICS in Systems with Multiple Populations of Oligomers*

When more than one population of fluorescent particles are present (e.g., monomers, dimers, and tetramers),  $\mathbf{g}(\mathbf{0}, \mathbf{0}, \mathbf{0})_t$  can be interpreted as:

$$\mathbf{g}(\mathbf{0}, \mathbf{0}, \mathbf{0})_t = \frac{\sum_i \bar{N}_i (\sigma_i^2 + \mu_i^2)}{\bar{N}_m^2} \quad (10)$$

where the sum is over all fluorescent species in the system,  $\bar{N}_m$  is the average number of monomers in the beam volume,  $\bar{N}_i$  is the average number of the  $i$ th species of aggregate in the volume, which has a mean number of monomers  $\mu_i$  and a variance in the number of monomers  $\sigma_i^2$  [12]. Equation 10 assumes that there is no quenching between the fluorophores in an aggregate. If quenching were present, the measured  $\mu_i$  would be lower than the true value, and it would appear as if fewer monomers were present in each aggregate. Unless simplifying assumptions can be made or additional information about the system is available from outside sources, it is usually impossible to apply the multiple parameter dependent Eq. 10 to single ICS measurement, since only one parameter is determined from the experiment (the correlation function magnitude,  $\mathbf{g}(\mathbf{0}, \mathbf{0}, \mathbf{0})_t$ ).

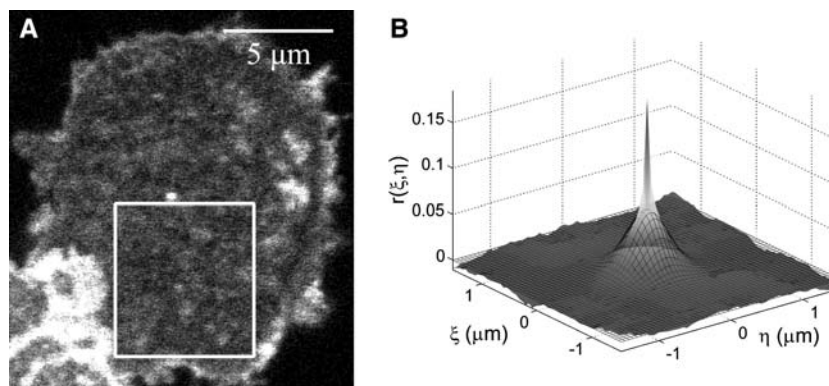


**Fig. 2** (A) Confocal laser scanning image of CHO K1 cell expressing EGFR-eGFP. (B) Spatial autocorrelation function for the region outlined in (A). The raw correlation function is given by the colored surface, and the fitted 2D Gaussian function is denoted by the black

mesh. The amplitude of the correlation function is the key parameter recovered from the fit, and it is inversely proportional to the number of independent fluorescent particles. From Ref. [23], with permission

Rocheleau et al. [28] developed an extension of ICS, which allows the fluctuations in an image associated with brightest aggregates to be separated from those of dimmer aggregates. The technique involves the sequential subtraction of intensity from LSM images, and is similar to that implemented by Wiseman et al. [29] to measure dendritic spine densities.

Ideally, one could determine the entire distribution of aggregation states, and not only the brightest aggregates (as in [28]), or a weighted average of the distribution (cf. Eq. 10). Such a determination is, in theory, possible. The full distribution of particle aggregation states can be calculated using higher order correlation functions, in which the relative number densities and brightnesses of species are measured (as demonstrated for FCS in [30]). This technique has been successfully applied to IgE distributions on supported planar membranes [31], in which the parameters extracted from the analysis qualitatively agreed with a visual inspection of the image. The accuracy and dynamic range of a related image moment technique applied to two-population systems was investigated by Sergeev et al. [32], who used it to measure oligomer distributions of imaged platelet-derived growth factor receptors (PDGF- $\beta$ R) in fixed cells. They found that the density of the oligomeric population should not be higher than the monomer density, and that the monomer concentration should not be higher than an order of magnitude greater than the oligomeric population in order to extract accurate results from the image moment analysis. They also measured a tetrameric state for the PDGF- $\beta$ R in agreement with ICS studies [22].

#### *Accuracy and Precision of Spatial ICS*

Costantino et al. [23] used computer simulations to determine the factors that affect the accuracy and precision of ICS measurements. They found that the two most important parameters are the number of sample laser beam areas in an image (i.e., the number of spatial intensity fluctuations) and background noise. The first criterion can be optimized by analyzing the largest homogeneous region in the sample. Although ICS can be performed on regions as small as  $16 \times 16$  pixels<sup>2</sup> ( $\sim 1.5 \mu\text{m}^2$ ), larger regions will yield more accurate results. The whole region of analysis should be “on cell,” since discontinuities in fluorescence, such as those caused by the edge of a cell, can introduce significant perturbations in the correlation function and its fit (see Section “Practical Guidelines for ICS Analysis”). In most cell measurements, background noise is the most important source of error, and can be minimized by the careful adjustment of microscope detectors, and a calibration of the fluorescence level from a monomeric unit of fluorophore either immobilized in a solid matrix or

adsorbed on a coverslip (if possible within the detection limits of the microscope). It is of paramount importance to subtract the correct amount of background intensity from the data before the analysis to obtain an unbiased estimate of the number density. This background correction has been discussed for both single measurements [23] and population averages [22]. Both autofluorescence from within the cell and non-specific antibody labeling in the extracellular environment can contribute intensity counts to an image. Both of these effects can be corrected for in ICS measurements [22]. Photon counting head detectors usually have greater sensitivity than analog photomultiplier tubes typically found on confocal microscopes. However, the latter type of detectors are satisfactory for ICS measurements as long as they are operated in a linear regime.

The statistics of ICS measurements have also been examined from a theoretical statistics perspective [33].

#### *Temporal Image Correlation Spectroscopy*

Spatial ICS can measure the number density and aggregation state of fluorescently labeled macromolecules. However, spatial ICS cannot extract dynamics because it only analyzes the spatial fluctuations in an image. Temporal image correlation spectroscopy (TICS) was introduced as an alternative to SFCS and FCS for slow moving membrane proteins which allows the diffusion coefficient and flow speed to be measured from an image time series [25, 34]. Time correlation functions are sensitive to moving fluorescent particles if they stay within the area defined by the beam for a number of image frames. Both the transport mode and rate of the particles are manifested in the time correlation function.

TICS has also been referred to in the literature as image cross-correlation spectroscopy [34, 35] and dynamic image correlation spectroscopy [36]. We prefer to exclusively use the term TICS to refer to the technique described here, since “cross-correlation” often implies measurements with two different color detection channels.

The normalized intensity fluctuation temporal autocorrelation function of an image series as a function of time lag  $\tau$  is obtained from Eq. 1 when  $\xi$  and  $\eta = 0$ :

$$r(0, 0, \tau) = \frac{\langle \delta i(x, y, t) \delta i(x, y, t + \tau) \rangle}{\langle i(x, y, t) \rangle_t \langle i(x, y, t + \tau) \rangle_{t+\tau}} \quad (11)$$

where the angular brackets denote spatial and temporal averaging. Experimentally,  $\tau$  values are determined by the time between subsequent images in the image series. Depending on the microscope system used,  $\Delta\tau$  is usually between 0.03 and 10 s. As we will discuss in Section “Raster Image Correlation Spectroscopy,” the imaging rate

must be appropriately matched to the time scale of the process of interest. An image series is discrete in both space and time, so a discrete approximation of the temporal autocorrelation function is calculated as follows:

$$r(0, 0, s) = \frac{1}{N-s} \sum_{c=1}^{N-s} \frac{1}{XY} \sum_{x=1}^X \sum_{y=1}^Y \frac{\delta i(x, y, c) \delta i(x, y, c+s)}{\langle i(x, y, c) \rangle_c \langle i(x, y, c+s) \rangle_{c+s}} \quad (12)$$

where  $X$  and  $Y$  are the number of pixels spanning the region being analyzed,  $N$  is the number of images in the image series,  $s$  is the discrete analog of  $\tau$ , and  $c$  is a dummy variable. The temporal correlation function calculated by Eq. 12 is then fit to the analytical decay model derived for the mode of transport present in the sample. Generally speaking, there are usually three parameters of interest determined from a time correlation function: its *amplitude*, which is inversely proportional to the number of particles (cf. Eq. 4); its decay *shape*, which describes the mode of transport the sample is undergoing (e.g., diffusion or flow); and its *rate of decay*, which describes how quickly the dynamic process is occurring.

For samples with 2D diffusion of the fluorescent particles, the temporal correlation function has the following decay form [8] (fit parameters in bold):

$$r(0, 0, \tau) = \mathbf{g}(\mathbf{0}, \mathbf{0}, \mathbf{0}) \left(1 + \frac{\tau}{\tau_d}\right)^{-1} + \mathbf{g}_\infty \quad (13)$$

where  $\mathbf{g}(\mathbf{0}, \mathbf{0}, \mathbf{0})$  is the zero-lags amplitude,  $\mathbf{g}_\infty$  is the long-time offset, and for confocal excitation, the characteristic diffusion time,  $\tau_d$  is related to the diffusion coefficient,  $D$  by:

$$D = \frac{\langle \omega_0 \rangle}{4\tau_d}. \quad (14)$$

The mean fit  $e^{-2}$  radius,  $\langle \omega_0 \rangle$ , for a particular analysis is usually determined by fitting the spatial autocorrelation function of each image to Eq. 9 and finding the average value of  $\omega_0$  for the time series [37]. As with spatial ICS (Section “Image Correlation Spectroscopy”), the value of  $\omega_0$  from the fits should be close to an independently measured value.

The correlation decay model of a sample with 2D flow is [10]:

$$r(0, 0, \tau) = \mathbf{g}(\mathbf{0}, \mathbf{0}, \mathbf{0}) \exp \left[ -\left(\frac{\tau}{\tau_f}\right)^2 \right] + \mathbf{g}_\infty \quad (15)$$

where the characteristic flow time,  $\tau_f$ , is used to calculate the flow speed,  $|v|$ :

$$|v| = \frac{\langle \omega_0 \rangle}{\tau_f}. \quad (16)$$

In the case where one population of particles simultaneously undergoes flow and diffusion, the autocorrelation function has the decay model:

$$r(0, 0, \tau) = \mathbf{g}(\mathbf{0}, \mathbf{0}, \mathbf{0}) \left(1 + \frac{\tau}{\tau_d}\right)^{-1} \exp \left[ -\left(\frac{\tau}{\tau_f}\right)^2 \right] + \mathbf{g}_\infty. \quad (17)$$

If there are two populations in the sample, with one undergoing diffusion and the other flow, the decay model is:

$$r(0, 0, \tau) = \mathbf{g}_1(\mathbf{0}, \mathbf{0}, \mathbf{0}) \left(1 + \frac{\tau}{\tau_d}\right)^{-1} + \mathbf{g}_2(\mathbf{0}, \mathbf{0}, \mathbf{0}) \exp \left[ -\left(\frac{\tau}{\tau_f}\right)^2 \right] + \mathbf{g}_\infty. \quad (18)$$

The ability to resolve multiple populations in a sample is dependent on a number of factors including the relative concentrations and quantum yields of the different species. Although these limitations of ICS have not been studied, there has been an extensive investigation of the analogous restrictions in the context of FCS measurements [38].

The percentage of the population which is immobile can be calculated from the offset parameter  $\mathbf{g}_\infty$  and the amplitude,  $\mathbf{g}(\mathbf{0}, \mathbf{0}, \mathbf{0})$ , obtained from the fits (Eqs. 13, 15, 17, or 18) [4]:

$$\% \text{ immobile} = \frac{\mathbf{g}_\infty}{\mathbf{g}_\infty + \mathbf{g}(\mathbf{0}, \mathbf{0}, \mathbf{0})}. \quad (19)$$

There is evidence that the detection of an immobile fraction using fluorescence recovery after photobleaching (FRAP) is an artifact caused by anomalous subdiffusion [39]. This effect has not been examined in the context of TICS measurements, and it is possible that the long-time offset of a temporal autocorrelation function reflects anomalous subdiffusion occurring in the system instead of an immobile population.

Finally, assuming the laser excitation volume has a 3D Gaussian intensity profile, the functional form of the time correlation function for a system with 3D diffusion is [40]:

$$r(0, 0, \tau) = \frac{\mathbf{g}(\mathbf{0}, \mathbf{0}, \mathbf{0})}{\left(1 + \frac{\tau}{\tau_d}\right) \left(1 + \frac{\langle \omega_0 \rangle^2 \tau}{\langle z_0 \rangle^2 \tau_d}\right)^{1/2}} + \mathbf{g}_\infty \quad (20)$$

where  $\langle z_0 \rangle$  is the mean  $e^{-2}$  radius of the laser focus in the axial direction. In practice,  $\langle z_0 \rangle$  (and  $\langle \omega_0 \rangle$ ) can be obtained by 3D optical sectioning of a sample of sub-diffraction-limit fluorescent microspheres distributed on a glass coverslip. Experimental temporal autocorrelation

functions for diffusing and flowing microsphere samples are presented in Fig. 3, along with fits to Eqs. 20 and 15.

### *Comparison of TICS, Fluorescence Recovery after Photobleaching, and Single Particle Tracking*

In addition to TICS, a number of other techniques have been developed to measure membrane dynamics, including SPT and FRAP. We will briefly discuss their relative advantages and disadvantages. SPT follows the location of one particle as a function of time to discern its mode of transport and diffusion coefficient or flow speed. Because the behavior of each particle is measured, subpopulations of particles can be clearly resolved [41]. In contrast, fluctuation correlation methods such as FCS and ICS measure, by their nature, an ensemble of particles and often report an average value, but not its distribution. Unlike single molecule techniques, such as SPT, fluctuation techniques may not be able to detect a subpopulation made up of a small fraction of the particles [38]. However, correlation techniques are generally more straightforward, and less time-consuming to implement (see supplemental material in [42]

for a comparison of SPT and ICS). Another key advantage of fluctuation techniques is that they can be applied to both relatively low and high density samples [43], unlike SPT which requires individual particles to be well separated. This need for low-density labeling is often incompatible with GFP transfections of proteins expressed at native levels in cells where individual fluorophores are not well resolved. Because SPT requires a low-density, high quantum-yield fluorophore, quantum dots (QDs) or colloidal gold particles are often used to label proteins of interest [44]. However, most methods of labeling a cell surface protein with these probes involve multivalent ligands, which can lead to unintended clustering of proteins and a concomitant erroneous determination of the macromolecule's dynamics [41, 44].

FRAP monitors the spontaneous recovery of fluorescence in a region of the cell membrane after all fluorophores in the region have been bleached with a laser pulse [45]. FRAP is capable of determining both the diffusion coefficient and immobile fraction of a system of fluorescently tagged molecules [46]. However, the technique requires the introduction of a large external perturbation by using high intensity laser illumination. Some studies have suggested this light can potentially injure the cell or induce cross-linking of membrane receptors [47, 48], but the general consensus is that there is no such damage [49, 50]. In contrast, TICS uses a much lower laser excitation power, and studies the system at equilibrium or biological steady state.

Data in FCS and FRAP experiments are sometimes fit to anomalous subdiffusion models [39, 51], in which particles exhibit a restricted mobility, but are not immobilized. It is thought that this non-Brownian behavior is the result of fixed obstacles or lipid rafts in the membrane [52]. To date, TICS data have not yet been fit to anomalous subdiffusion models, and it would be beneficial to study systems with a number of techniques and over a range of time scales.

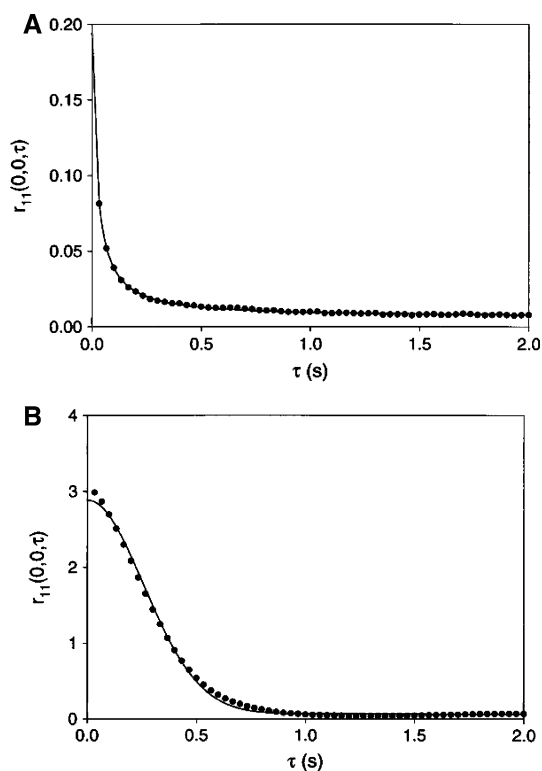


**Fig. 3** Temporal image correlation decays for fluorescent microspheres in aqueous sucrose solution, imaged on a two-photon laser scanning microscope, undergoing (A) diffusion and (B) flow. From Ref. [25], with permission

### *Accuracy of, and Photobleaching in, TICS*

Kolin et al. [43] examined the accuracy of TICS measurements by using computer simulations of LSM imaging of point emitters undergoing diffusion and flow. They found that, as with spatial ICS, recovering accurate number densities from TICS autocorrelation functions was primarily limited by background noise in the sample. In contrast, diffusion coefficients and flow speeds could be recovered in the presence of high levels of background noise, and their accuracy was governed by spatiotemporal sampling (i.e., the number of pixels in the region of analysis, and the number of frames in the image time series). The effect of photobleaching on temporal autocorrelation



function decays was also studied in the same work, and it was found to cause a severe underestimation in number densities (by approximately a factor of 5), and a smaller, but still significant, overestimation of diffusion coefficients and flow speeds (roughly 20% for diffusion, and 5% for flow). For the case of irreversible monoexponential photobleaching, the authors provide a correction factor which can be used when fitting the data to recover unbiased values of  $\langle n_p \rangle$ ,  $D$ , and  $v$ .

Cytosolic fluorophore populations should not interfere with TICS measurements of fluorescently labeled membrane proteins. Since proteins in the cytosol diffuse approximately two orders of magnitude faster than membrane-bound proteins, any concentration fluctuations due to fluorophores in the cytosol will be completely decorrelated in subsequent images, which are typically acquired at imaging rates below 10 Hz. Although the dynamics of these quickly diffusing species cannot be measured from LSM-acquired image series using TICS, we will describe a novel extension of ICS in Section “Raster Image Correlation Spectroscopy” that can measure such faster transport processes.

### Image Cross-Correlation Spectroscopy

Image cross-correlation spectroscopy (ICCS) quantifies the coincident spatial fluctuations of two images collected in two different detection channels. Usually, two fluorophores with different emission wavelengths are attached to two different proteins of interest. The two fluorophores are imaged on a microscope that spectrally resolves the emissions, and an image is collected for each detection channel:  $i_a(x, y)$  and  $i_b(x, y)$ . The normalized intensity 2D spatial cross-correlation function for these two images is given by Eq. 1 with  $\tau = 0$ :

$$r_{ab}(\xi, \eta) = \frac{\langle \delta i_a(x, y) \delta i_b(x + \xi, y + \eta) \rangle}{\langle i_a(x, y) \rangle \langle i_b(x, y) \rangle}, \quad (21)$$

and is calculated using Fourier methods, just as with a spatial autocorrelation function (Eq. 8). The average number of colocalized independent fluorescent particles in the beam area,  $\langle n_{ab} \rangle$  is:

$$\langle n_{ab} \rangle = \frac{g_{ab}(0, 0)}{g_{aa}(0, 0)g_{bb}(0, 0)}, \quad (22)$$

where  $g_{ab}(0, 0)$  is the amplitude of the cross-correlation function, and  $g_{aa}(0, 0)$  and  $g_{bb}(0, 0)$  are the amplitudes of the autocorrelation functions for channels  $a$  and  $b$ , respectively. All three amplitudes are determined by nonlinear curve fitting of their respective correlation functions to Eq. 9. The number density  $\langle n_{ab} \rangle$  is usually transformed to a CD

(as in Eq. 5), or the fraction of protein 1 interacting with protein 2 (or vice-versa) using  $\langle n_a \rangle$  or  $\langle n_b \rangle$ .

A dual-labeled sample can be imaged as a function of time, and the fluorescence emissions imaged simultaneously in two detection channels to generate a dual-color image time series. A temporal cross-correlation function can be calculated from this image series, which is given by Eq. 1 with the spatial-lag variables  $\xi$  and  $\eta$  set to zero:

$$r_{ab}(0, 0, \tau) = \frac{\langle \delta i_a(x, y, t) \delta i_b(x, y, t + \tau) \rangle}{\langle i_a(x, y, t) \rangle_t \langle i_b(x, y, t + \tau) \rangle_{t+\tau}}. \quad (23)$$

If a fraction of the two populations are interacting on the time scale of the measurement,  $r_{ab}(0, 0, \tau)$  can be fit to the same analytical models as the temporal autocorrelation decays (e.g., Eqs. 13, 15, 17, or 18 or 20) to determine the dynamics of the interacting complex. If there is no interaction between the species, the cross-correlation function will be zero for all  $\tau$  if sampling of fluctuations is sufficient.

### Advantages, Limitations, and Dynamic Range of ICCS

As alternatives to ICCS, protein–protein interactions can also be measured using automatic colocalization algorithms [53, 54]. These techniques calculate the interaction fraction for two protein species separately labeled with different color fluorophores based on the amount of signal overlap between pixels at the same image location for the two detection channels. Comeau et al. [55] and Costantino et al. [23] extensively studied the accuracy of ICCS and compared it to the automatic colocalization algorithms commonly found in commercial microscope software, and found the two techniques were complimentary and delivered accurate results under different experimental conditions. Specifically, spatial ICCS is able to accurately determine the fraction of proteins interacting over several orders of magnitude in concentration. In contrast, automatic colocalization usually provides accurate estimates at low fluorophore density, but can overestimate the fraction of interacting protein at higher concentration levels. Furthermore, spatial ICCS only works well when the interaction fraction is higher than 20% (for a typical image size of  $256 \times 256$  pixels), while automatic colocalization will return an erroneous result if there is more than a factor of 2 difference between the concentration of the two populations being measured. Also, ICCS is substantially less affected by the signal-to-noise of the images than automatic colocalization algorithms [55].

An advantage of ICCS is its ability to automatically correct for different spatial alignments of the two channels. Chromatic aberrations in microscope objectives,

misalignment of optical components, and vibrations and mechanical instability of the scanning system can all cause a shift of more than one pixel between two color images acquired from the same sample [56]. Automatic colocalization techniques are greatly affected by systematic shifts since they directly compare pixels at the same image coordinate, so the raw data must be appropriately corrected for this shift. Although more sophisticated colocalization implementations include this pre-registration (such as the Medical Image Processing, Analysis, and Visualization (MIPAV)) software package developed by the Center for Information Technology, National Institutes of Health [57]), most do not automatically account for this shift. In contrast, a spatial shift between two images used for cross-correlation analysis would simply introduce a shift in the location of the cross-correlation function maximum, but would not alter the key parameter, its amplitude [55].

Automatic colocalization algorithms require that both channels in the optical setup have the same PSF [54], while cross-correlation calculations can be corrected for PSFs of different sizes [55, 58]. Additionally, the automatic colocalization algorithms force each pixel to be classified as either colocalized or non-colocalized, in contrast to ICCS, which takes into account that the PSF convolution causes intensity counts to be present in pixels adjacent to those where fluorophores are actually centered.

FRET has also been used to probe protein–protein interactions in live cells [59]. FRET measures the amount of non-radiative energy transfer between a donor and an acceptor fluorophore. In vitro measurements can give accurate distance measurements on the order of 1–10 nm, while measurements in live cells typically detect either the presence or absence of the transfer. Unlike FRET, cross-correlation cannot determine the average separation between two fluorophores. It can only give the fraction of the labeled species, which are located together spatially or travel together temporally in a common complex. However, some biomacromolecular complexes are so large that FRET cannot be used to measure the separation between two different components on opposite sides of the aggregate. Also, ICCS and automatic colocalization would find two components colocalized if they were in a common subcellular compartment, whose size was below the diffraction limit ( $\sim 200$  nm) and were imaged in the same pixel location. On the other hand, FRET could be used to differentiate between a true close interaction between two components, and a common compartmentalization.

As with ICS, the images analyzed must be relatively homogeneous, and without sharp bands of intensity or discontinuities. For example, ICS and ICCS may be appropriate for studying transmembrane proteins in the plasma membrane, but not the trans-Golgi network. Also,

spectral bleed-through of signal (also known as cross-talk) between the detection channels must be corrected for to prevent artifacts in ICCS analyses.

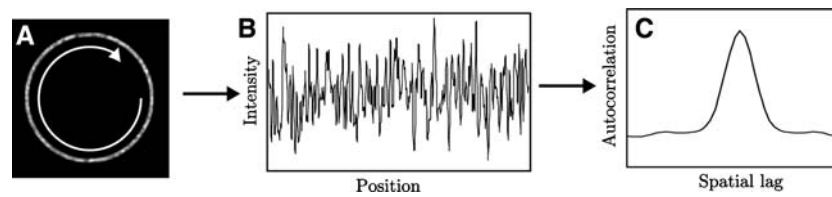
### Correlation Techniques for Non-Planar Regions of Cells

Image correlation techniques assume that the imaged membrane is perfectly flat. A small slope or undulations in the membrane would perturb the correlation functions. Petersen [12] examined the effect of a sloped membrane on spatial ICS measurements using simulations and found that while the  $g(0,0,0)_t$  value is not significantly affected, a degree of aggregation calculation (cf. Eq. 6) would be underestimated. The membrane slope causes this effect because the out-of-focus membrane contributes less to the intensity, and  $\langle i \rangle$  is lower than if the membrane were entirely in focus. Milon et al. [60] investigated the effect of sloped, out-of-focus, or undulating membranes on FCS autocorrelation functions using simulations and measurements on large unilamellar vesicles, and found that these membrane characteristics could cause the diffusion coefficient to be underestimated by approximately a factor of 3 in FCS measurements on typical cells.

Some cell lines, such as leukocytes, are spherical and do not have flat areas appropriate for traditional ICS analysis. In this situation, a cell can be imaged on a LSM and using the microscope's inherent optical sectioning capability, and a z-slice can be obtained from an axially central region, in which neither the basal nor the apical membranes are visible yielding an image with “ring” staining for a membrane protein. Afterwards, a fluorescence trace around this “ring” can be extracted. This fluorescence record has been used to measure colocalization using a cross-correlation approach [61–63], as well as dynamics using a modified TICS analysis [64]. This technique is summarized in Fig. 4. A line trace around the perimeter of a cell membrane samples far fewer fluctuations than an image of a planar region of the membrane; therefore, these variants have an inherently lower signal-to-noise ratio than their imaging counterparts, and are best suited to round cell types which lack a large, relatively flat membrane region.

### Spatiotemporal Image Correlation Spectroscopy

TICS is able to measure the *magnitude*, but not the *direction* of a concerted flux of flowing fluorophores (i.e., the flow speed). As first suggested in [65], the direction of the flow can be determined by calculating a full spatiotemporal correlation function. The technique was later fully developed and verified, and was named spatiotemporal ICS



**Fig. 4** An overview of ring correlation spectroscopy (RCS). **(A)** The image series collected in time from an optical section of the entire “spherical cell” at its equator. The resulting image series contains intensity rings for labeled membrane species. **(B)** In RCS, the intensity trace around the cell membrane is extracted for each image

in the time series. **(C)** These membrane perimeter intensity records are correlated in space (for each ring) as well as time for a given membrane pixel location to measure the number density, dynamics, or interacting fractions of the fluorescently labeled proteins

(STICS) [20]. Recently, a similar technique has also been developed independently [66]. The theory of STICS analysis is similar to particle image velocimetry (PIV), a technique developed in 1984 to measure the turbulent flow of non-fluorescent micron-sized beads in fluids [67]. However, STICS incorporates greater temporal lag sampling into the calculation of the space–time correlation function from which velocity vectors are measured.

A spatiotemporal correlation function is defined in Eq. 1. As with ICS autocorrelation functions, this function is usually calculated with FFTs using the Wiener-Khinchin theorem (Eq. 8), because using the FFT is several times

faster than the “direct” calculation [17]. The point spread function of laser scanning and TIRF microscopes is approximately Gaussian in the axial plane, so a STICS correlation function is usually a 2D Gaussian which moves from the zero-lags center as a function of time lag if there is a flow present (Fig. 5A(ii)). The velocity of the sample is determined by tracking the center of the moving peak at each time lag. Linear regressions of the  $x$ - and  $y$ -coordinates of the peak location as a function of time yield the  $x$ - and  $y$ -components of the velocity for uniform motion (Fig. 5C) [20]. As with PIV, using FFTs can introduce a significant bias in the correlation function if the PSF is on

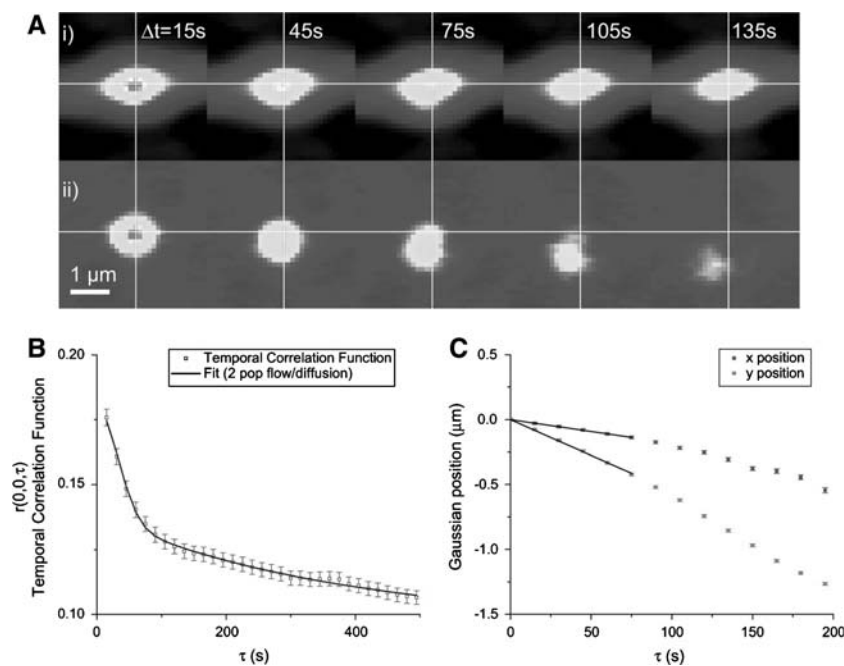


**Fig. 5** STICS **(A, C)** and TICS **(B)** analysis of a region of the basal membrane of a living CHO cell expressing  $\alpha$ -actinin-eGFP. The spatiotemporal correlation function without immobile population removal **(A(i))** does not show a clear flowing population because the flowing component is masked by a slowly diffusing or immobile component. However, when the immobile filtering is applied **(A(ii))**, a flowing component becomes readily visible, and is easily tracked in the STICS correlation function. This peak location is tracked, and a

linear regression of each of the  $x$  and  $y$  peak positions as a function of time lag,  $\tau$ , gives the velocity vector components  $v_x = (1.8 \pm 0.3) \times 10^{-3} \mu\text{m/s}$  and  $v_y = (5.5 \pm 0.2) \times 10^{-3} \mu\text{m/s}$ , respectively **(C)**. TICS analysis of the same region yields a temporal autocorrelation function best fit by a two-population flow/diffusion model, giving  $v_{\text{ICS}} = (7.7 \pm 0.8) \times 10^{-3} \mu\text{m/s}$  and  $D = (6 \pm 1) \times 10^{-5} \mu\text{m}^2/\text{s}$ . From Ref. [20], with permission

the order of the size of the window used in STICS analysis [68]. This regime is usually not encountered with typical applications of STICS.

As with ICS, a STICS analysis is usually performed on different subregions of a cell (e.g., Fig. 6B). In the most recent application, a high-resolution variant has been used in which many small, partially overlapping regions are analyzed on the same sample (usually areas of  $16 \times 16$  pixels<sup>2</sup>, where each new region is offset 4 pixels from an adjacent region; see Fig. 7).

In many biological systems, two different proteins may interact periodically, but are not always colocalized. In such a case, a STICCS cross-correlation analysis will not yield a measurable Gaussian peak, because the correlation decays too quickly. In these situations, vector maps from each individual channel can be calculated (Fig. 7). The interaction between the two different proteins can then be quantified by comparing the relative magnitude and orientation of corresponding vectors in the velocity maps [69]. Brown et al. [69] hypothesize that this data treatment reveals the transient interaction between two different proteins because the binding and unbinding will lead to a fractional correlation in the two velocities. This method of analyzing dual-color STICS vector maps is thus a useful way to quantify transient protein–protein interactions when there is not a measurable cross-correlation.

#### Immobile Population Removal

The STICS theory presented to this point assumes there is only one population of fluorophores, which is flowing. However, in living cells, there is often a significant fraction of labeled protein that is either slowly diffusing or immobile in the plasma membrane on the measurement time scale. Either of these non-flowing populations, if

present, are manifested in the STICS correlation function, and can prevent an accurate tracking of the flow correlation peak (Fig 5A(i)) [20].

The immobile population is usually removed from an image series prior to STICS analysis by subtracting the “mean image” of the image series from each image. This can be accomplished quickly by Fourier transforming in time each pixel trace in the image series, setting the DC component of the transforms to zero, and inverse Fourier transforming each pixel trace to recover the original movie with only the moving components preserved [20].

Slowly diffusing particles will also create a central lags peak in the STICS correlation function, which can mask the flow correlation peak which must be well-resolved to be tracked and to recover an accurate velocity. Using the previously described Fourier-based immobile population removal will only partially eliminate the contribution of the diffusing population to the correlation function [20]. An alternative method of removing slowly moving features in an image series is to use a moving average filter [70]. The variable temporal window size used in the filter determines which features are removed.

#### k-Space Image Correlation Spectroscopy

Concentration correlation techniques measure the underlying dynamics of a system by calculating a correlation function of spontaneous fluctuations observed as fluorophores move in and out of a small observation volume. To extract meaningful dynamics such as the diffusion coefficient or flow speed, these correlation functions are fit to different analytical models depending of the type of transport process the fluorophores are undergoing (e.g., Eqs. 13 and 15 for diffusion and flow, respectively). These analytical functions were derived assuming that the

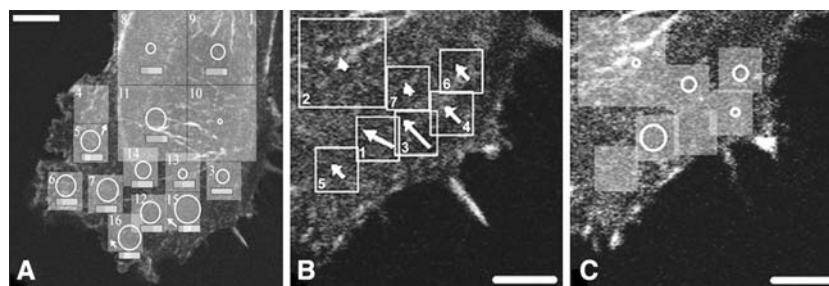


**Fig. 6** (A) Dynamics of  $\alpha$ -actinin-GFP fusion proteins in a live CHO-B2 cell, imaged on a two-photon LSM, were measured using TICS and STICS analysis. The region of the cell beneath area “3” in (A) was analyzed in more detail both before (B) and after (C) retraction of a microspike. There was a concerted flux of  $\alpha$ -actinin away from the microspike during the retraction (B), while only diffusion was detected in those regions after the retraction (C). Circles indicate the

average 10 min root-mean-square diffusion distance from the center of the circle. Arrows give the direction and average 10 min displacement for proteins undergoing flow in a particular region, as determined using STICS. The pixel size in all three image series was  $0.118 \mu\text{m}$ , and images were acquired at 5 s intervals. Scale bars are  $10 \mu\text{m}$  (A) and  $5 \mu\text{m}$  (B and C). From Ref. [4], with permission



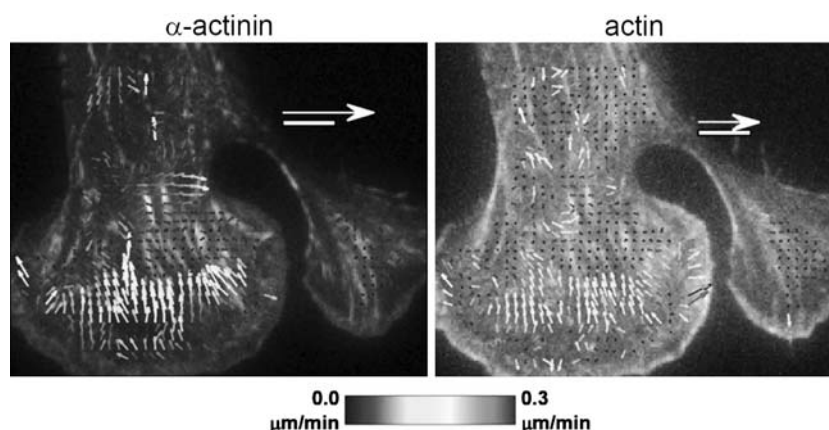


**Fig. 7** High-resolution velocity maps of  $\alpha$ -actinin-eGFP and actin-mRFP in an MEF cell plated on 1  $\mu$ g/ml fibronectin. Image series were acquired on a TIRF microscope (Olympus IX70) with a Retiga EXi CCD camera. The color scale is common between both maps (see colorbar below images). The length scale of the velocity arrows varies between both maps; in both cases the velocity scale arrow represents

0.5  $\mu$ m/min, and the spatial scale bar is 5  $\mu$ m. Each analysis used 100 images, acquired at intervals of 10 s, with a pixel size of 0.215  $\mu$ m. The relative directional correlation and relative velocity magnitude between both maps can be calculated. From Ref. [69], with permission

movement of fluorophores is the only process causing fluctuations in the collected fluorescence [8, 10]. However, many fluorophores have time dependent photophysical properties, such as fluorophore photobleaching [71] and intermittent fluorescence or “blinking” [72]. In fluorescence correlation techniques such as FCS and TICS, these intensity fluctuations due to the fluorophore photophysics must be taken into account when fitting the decay with an analytical model. If not, the experimental autocorrelation function may appear to be fit well by a model which only accounts for transport, but the transport coefficients recovered may be highly erroneous [43, 73].

Blinking of organic fluorophores occurs on the microsecond time scale, and is not sampled in the TICS autocorrelation functions because it occurs much faster than the imaging rate; any correlations due to triplet state photophysics are completely lost by the time a subsequent image is acquired. As described for TICS in Section “Accuracy of, and Photobleaching in, TICS,” photobleaching of organic fluorophores can significantly affect the diffusion coefficient and flow speed obtained from temporal autocorrelation functions. This perturbation can be corrected for by fitting to an analytical model, which takes into account a first-order photobleaching contribution to the correlation function [43]. However, fluorescent proteins can also undergo reversible photobleaching [71], and this behavior is not easily measured from an image series of a live cell or corrected for in TICS studies. As well, QDs have recently emerged as novel fluorescent tags for biological macromolecules. Unlike organic fluorophores, QDs exhibit greatly reduced photobleaching under continuous laser excitation for extended periods of time (minutes to hours) [74, 75]. However, they do

exhibit significant emission “blinking,” in which individual QDs alternate between “on” and “off” states [76]. In contrast to organic fluorophores whose “on” and “off” distributions are characterized by exponential distributions [72], those of QDs are governed by extended power-law distributions in time [77]. These power-law distributions do not have a characteristic (i.e., average) “on” or “off” time. There have been recent efforts to derive an analytical model for temporal autocorrelation functions of QD blinking [78, 79]. However, their results are very complex, have not been yet tested experimentally, and are not directly amenable to experimentally measured correlation functions for blinking and diffusing QDs.

k-Space image correlation spectroscopy (kICS) is a useful new image correlation technique applicable when fluorophores undergo significant photobleaching or “blinking,” because it always returns unbiased estimates of the fluorophore dynamics without any previous knowledge of the photophysics or PSF of the system [80]. As with the previously mentioned techniques, the seminal measurement in kICS is a microscope image time series,  $i(\mathbf{r}, t)$ . With kICS, each image is 2D Fourier transformed in space to yield  $\tilde{i}(\mathbf{k}, t)$ , before being correlated in time. (With modern computers, performing the transform prior to correlating imparts only a small increase in analysis time.) We define a reciprocal-space time correlation function,  $r(\mathbf{k}, \tau)$ , as:

$$r(\mathbf{k}, \tau) = \langle \tilde{i}(\mathbf{k}, t) \tilde{i}^*(\mathbf{k}, t + \tau) \rangle, \quad (24)$$

where the angular brackets denote a time average. The notation  $\tilde{i}^*(\mathbf{k}, t + \tau)$  denotes the complex conjugate of the



2D spatial Fourier transform of image  $i(\mathbf{r}, t + \tau)$ . Assuming the system is imaged on a microscope with a Gaussian PSF,  $r(\mathbf{k}, \tau)$  has the following form for a 2D system of a population of fluorescent particles undergoing diffusion and flow [80]:

$$r(\mathbf{k}, \tau) = N \frac{q^2 I_0^2 \omega_0^4 \pi^2}{4} \langle \Theta(t) \Theta(t + \tau) \rangle \times \exp \left[ i \mathbf{k} \cdot \mathbf{v} \tau - |\mathbf{k}|^2 \left( D\tau + \frac{\omega_0^2}{4} \right) \right], \quad (25)$$

where  $N$  is the number of particles in the image,  $q$  is the quantum yield,  $I_0$  is the incident laser central peak intensity,  $\mathbf{v}$  is the velocity of the particles, and  $\Theta(t)$  is 1 if a particle is fluorescing at time  $t$  and 0 otherwise. The angular brackets denote an average over all particles in the image. For a sample undergoing diffusion,  $D$  is calculated by circularly averaging  $r(\mathbf{k}, \tau)$  and taking the natural logarithm:

$$\ln[r(|\mathbf{k}|^2, \tau)] = \ln \left[ N \frac{q^2 I_0^2 \omega_0^4 \pi^2}{4} \langle \Theta(t) \Theta(t + \tau) \rangle \right] - |\mathbf{k}|^2 \left( D\tau + \frac{\omega_0^2}{4} \right). \quad (26)$$

Note that the first term is constant for a given value of  $\tau$ , and  $D$  can be extracted from  $\ln[r(|\mathbf{k}|^2, \tau)]$  with several linear regressions (Fig. 8). In contrast to r-space correlation techniques,  $D$  can be calculated without any knowledge of the fluorophore photophysics [80, 81]. An application of kICS to QD blinking is described in Section “Fluorophore Photophysics.”

We have recently shown that a new implementation of kICS can give a PSF-independent correlation function [81]. Therefore, kICS analysis does not require a calibration of the PSF of the imaging system, and automatically accounts for a non-Gaussian PSF, or an any asymmetry in the focal plane due to misalignment of optics.

One disadvantage of kICS is that it cannot be applied to arbitrarily small regions of cells. The analysis involves a linear regression (cf. Fig. 8), and depending on the sample size and noise level, a reliable fit may not be possible. Under typical imaging conditions, this usually limits analyses to image series  $32 \times 32$  pixels<sup>2</sup> or larger, precluding the study of small cells such as yeast or bacteria.

The theory of kICS is very similar to that of dynamic light scattering [82], however the instrumental implementation and systems studied vary significantly. Fink et al. [19] and Hattori et al. [83] have developed techniques similar to kICS to selectively probe wavevectors using two interfering laser beams. These techniques can recover the same quantities as kICS; however, they require specialized equipment and cannot be applied directly to image series acquired on commercial imaging microscope, as can kICS.

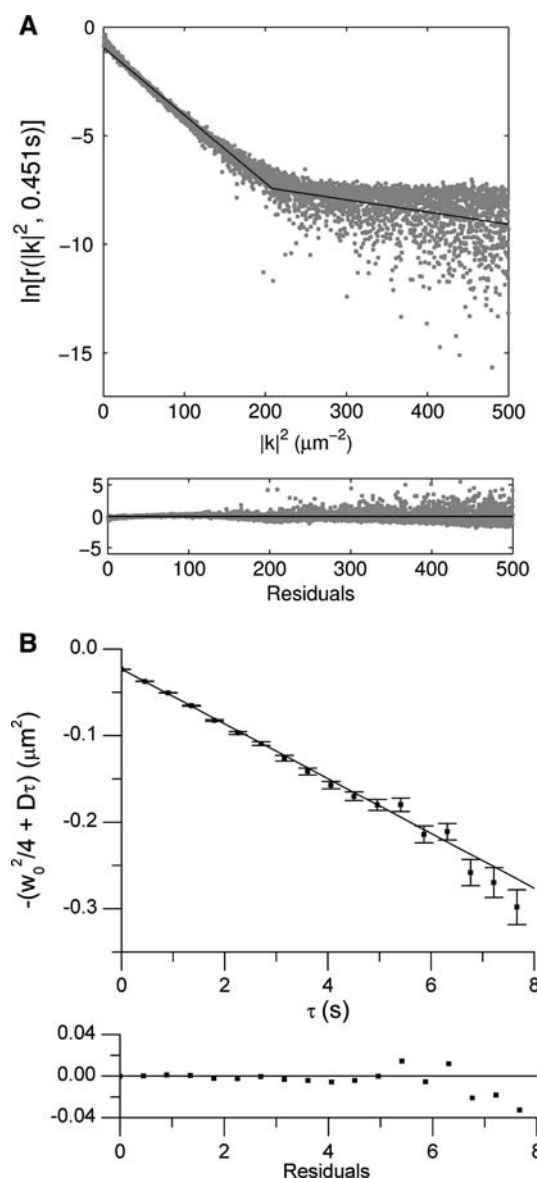


**Fig. 8** (A) The circularly averaged, natural logarithm of the  $k$ -space time correlation function at  $\tau = 0.451$  s for a sample of diffusing microspheres, with a radius of  $0.1 \mu\text{m}$ , in sucrose solution. The image series was acquired on a confocal laser scanning microscope. The intercept of the correlation function as  $|\mathbf{k}|^2 \rightarrow 0$  is proportional to the number of particles in the image, and is also dependent on the photophysics of the fluorophore. The slope of the first segment (i.e., at low  $|\mathbf{k}|^2$ ) is related to the diffusion coefficient (cf. Eq. 26). Noise is manifested in the second segment (i.e., at high  $|\mathbf{k}|^2$ ). An analogous regression is performed for  $r(\mathbf{k}, \tau)$  for each value of  $\tau$ . (B) The slopes obtained from the plots of (A) at different  $\tau$  values are plotted as a function of  $\tau$ , and the diffusion coefficient is given by this slope. In this case,  $D = (0.0316 \pm 0.0002) \mu\text{m}^2/\text{s}$ . From Ref. [80], with permission

### Raster Image Correlation Spectroscopy

For TICS and kICS analysis, the imaging rate of the microscope dictates the maximum rate of a diffusive

process which can be measured [43]. On a typical LSM, this limits the largest diffusion coefficient measurable to approximately  $10^{-9}$  cm<sup>2</sup>/s. Most membrane proteins diffuse more slowly than this, so applying TICS to image series collected on an LSM is often an appropriate method to study this phenomenon. However, small molecules or proteins in solution diffuse far too quickly to be studied using either TICS or kICS, because fluorophores enter and leave the small focal volume long before a subsequent image is acquired, so intensity fluctuations in adjacent images in the image series are completely uncorrelated. Until recently, these fast dynamics could only be measured using FCS, which is not included with most commercial LSMs. A new approach, raster image correlation spectroscopy (RICS) allows fast dynamics to be probed on standard LSMs, which are common in life science research environments.

Digman et al. [84, 85] developed RICS, which allows one to measure rapid diffusion on a commercial LSM analogous to what can be measured with single-point FCS. These microscopes generate an image by using galvanometer mirrors to raster a laser beam across a sample, recording one pixel at a time. The raster-scanning used to generate an image introduces a time structure into the image since different parts of the image are acquired at different times (Fig. 9). RICS can therefore measure the diffusion coefficient of a sample of fluorophores imaged on a LSM by taking advantage of spatial correlations due to the raster pattern in which the image is constructed.

As with spatial ICS, the RICS autocorrelation function of an image collected on a confocal or two-photon laser scanning microscope is defined as in Eq. 7. If particles diffuse significantly on the time scale of image acquisition, the spatial autocorrelation function will not have an isotropic Gaussian shape (cf. Eq. 9, Fig. 2B). Instead, it will be “stretched” out in the fast scan direction, and the diffusion coefficient may be extracted by taking into account

the time structure of the image introduced by the scanning mechanism (Fig. 10). In this case, the analytical form of the spatial autocorrelation function,  $G_s(\xi, \eta)$ , is:

$$G_s(\xi, \eta) = S(\xi, \eta) \times G(\xi, \eta) \quad (27)$$

where  $S(\xi, \eta)$  is the correlation function due to the scanning of the laser beam, and  $G(\xi, \eta)$  is the correlation function due to diffusion. Because the laser beam scanning and particle diffusion are independent processes, the correlation function  $G_s(\xi, \eta)$  (Eq. 27) is the product of the correlation function for each process. A number of analytical forms of  $S(\xi, \eta)$  exist for different scanning geometries [85]. When an image is collected on a commercial LSM, the laser is raster scanned across the sample line-by-line, and  $S(\xi, \eta)$  has the following form:

$$S(\xi, \eta) = \exp \left[ -\frac{\frac{\delta_r^2}{\omega_0^2} (|\xi|^2 + |\eta|^2)}{1 + \frac{4D(\tau_p|\xi| + \tau_1|\eta|)}{\omega_0^2}} \right] \quad (28)$$

where  $\tau_p$  is the pixel residence time,  $\tau_1$  is the line repetition time,  $\delta_r$  is the pixel size, and

$$G(\xi, \eta) = \frac{\gamma}{N} \left( 1 + \frac{4D(\tau_p|\xi| + \tau_1|\eta|)}{\omega_0^2} \right)^{-1} \times \left( 1 + \frac{4D(\tau_p|\xi| + \tau_1|\eta|)}{\omega_z^2} \right)^{-1/2} \quad (29)$$

where  $\gamma$  is a factor describing the geometry of the laser beam [86]. It should be noted that the spatial lag variables  $\xi$  and  $\eta$  in Eqs. 28 and 29 are in pixel units, and not microns as in Eq. 9.

As with STICS, an immobile or slowly diffusing population can mask the correlation function of interest [20, 85]. Therefore, when RICS is used to measure cytosolic dynamics in living cells, either a Fourier or moving average filter may be required [85] (Fig. 10).

**Fig. 9** (A) Dynamics of fluorophores attached to biomolecules ranging in size from small molecules to large protein aggregates in membranes can be measured using a LSM by applying a variety of correlation techniques. (B) An image series acquired on an LSM contains information on time scales from the microsecond to second regimes. Using RICS, it is possible to exploit this time structure to measure fast diffusion processes. From Ref. [85], with permission

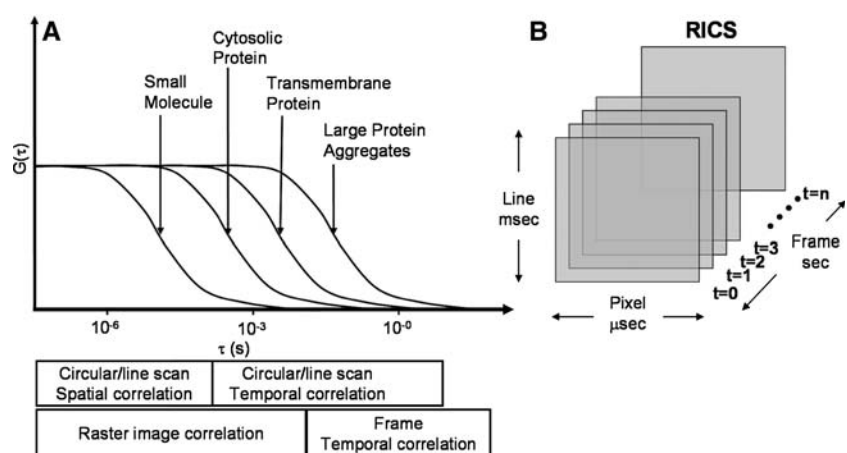
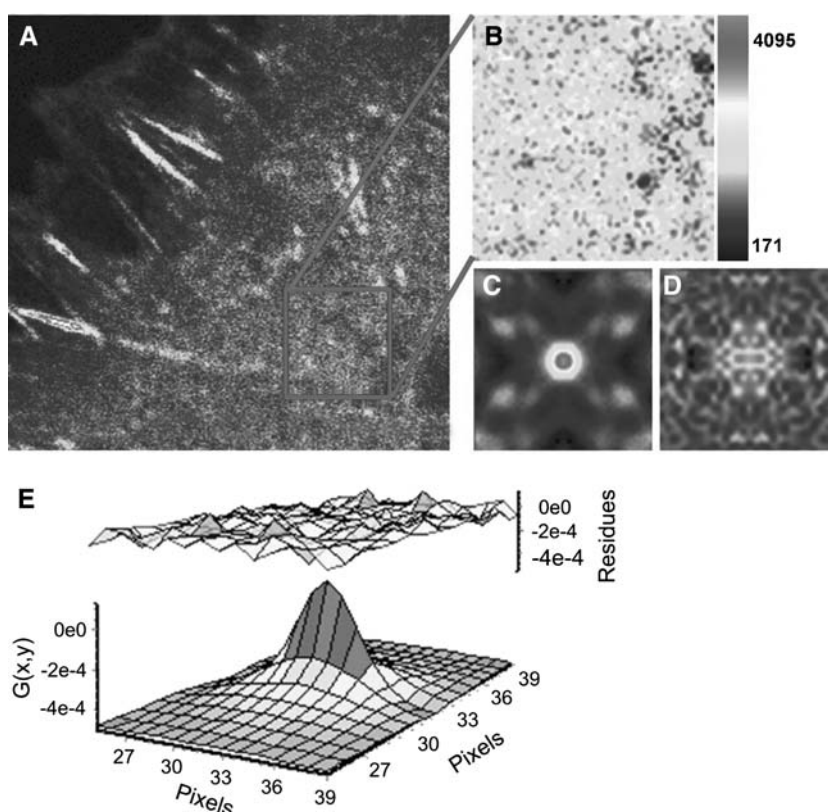


**Fig. 10** (A) An image of a CHO K1 cell transfected with a paxillin-eGFP fusion protein, imaged on a confocal LSM. (B) An enlargement of the  $64 \times 64$  pixel<sup>2</sup> region outlined in (A). The correlation function for the region shown in (B) both without (C) and with (D) immobile removal. (E) The correlation function in (D) was fit to Eq. 27, using Eqs. 28 and 29, giving  $D = 8.3 \mu\text{m}^2/\text{s}$ . The pixel dwell time was  $8 \mu\text{s}$ , the pixel size was  $0.09 \mu\text{m}$ , and the line scan time was  $5.05 \text{ ms}$ . To improve the measurement signal-to-noise, the average of correlation functions from 23 regions in identical locations in sequential images were used to calculate the correlation functions in (C) and (D). From Ref. [85], with permission



### Particle Image Correlation Spectroscopy

Semrau and Schmidt [87] recently introduced PICS, a hybrid technique, which contains elements of both image correlation and particle tracking. One step in SPT data analysis is linking particle positions in subsequent images into particle trajectories. This process can be a challenge at high densities, when the inter-particle spacing approaches the step size of particle movements. One limitation of ICS is its insensitivity to movements below the diffraction limit of the imaging system. The PICS technique avoids these two pitfalls and permits the measurement of arbitrarily high diffusion coefficients at high densities, as long as individual particles can be resolved. PICS involves first identifying individual particles in each image of an image time series. A temporal cumulative correlation function is then generated from these particle positions, and the diffusion coefficient is calculated from this correlation function. PICS provides an attractive alternative to other techniques when high fluorophore densities prevent SPT analysis, or dynamics which occur on a sub-diffraction-limit length scale preclude traditional ICS measurements.

### Software for ICS Analysis

To aid researchers in adopting ICS techniques, we have made MATLAB implementations freely available at

<http://wiseman-group.mcgill.ca/>. The software includes command-line implementations of ICS, TICS, STICS and a basic simulation program. A brief tutorial is included with the distribution. As well, a full-featured high-resolution STICS program is provided with a graphical user interface. For implementing techniques not provided at the above website, we recommend MATLAB or IDL as programming languages which are relatively easy-to-learn for those without formal programming training. Also, researchers may find the programs SimFCS and Globals for Imaging useful for FCS and RICS analysis. These programs are available at <http://www.lfd.uci.edu/globals/>.

### Practical Guidelines for ICS Analysis

The accuracy and precision of the results obtained from the techniques described in this review are strongly dependent on the quality of the data, which is analyzed. In Fig. 11, we present images, which are either acceptable or unacceptable for ICS analysis, and describe some of the most common pitfalls. Although microscopy techniques are beyond the scope of this review, some excellent guidelines for fluorescence microscopy of live cells in general are in Ref. [88], and for confocals specifically in Ref. [89].

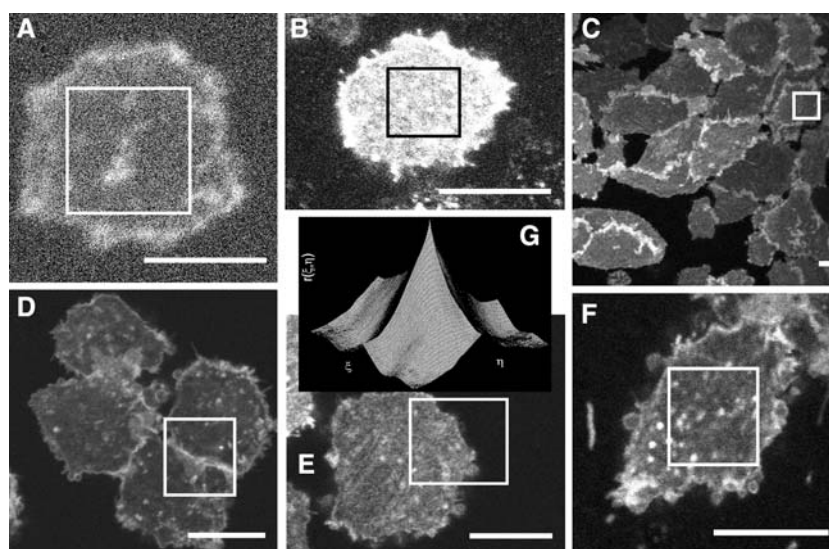


**Fig. 11** Some common pitfalls in collecting suitable images for ICS analysis are illustrated with a series of images of CHO cells transfected with EGFR-eGFP imaged using a confocal LSM (Olympus FV300 IX71, with 60X 1.4 NA oil objective, and 488 nm line of an Ar<sup>+</sup> laser for excitation). These specific guidelines are given in the context of spatial ICS, although most are applicable to all of the forms of correlation analysis mentioned in the review. **(A)** Too much noise prevents an accurate determination of number density, and can be improved by averaging multiple frames in the series, changing the collection filters used, and by increasing the labeling efficiency, fluorophore brightness, detector sensitivity, or excitation intensity. **(B)** Detector saturation perturbs a correlation analysis by clipping the positive fluctuations. It can be avoided by decreasing the excitation intensity or detector sensitivity. An analogous effect occurs with negative fluctuations when a microscope offset setting is used to discard low intensity values. When collecting images for ICS

analysis, the offset setting should be set to zero. **(C)** The microscope zoom used to collect this image gave a pixel size of  $\sim 0.5 \mu\text{m}/\text{pixel}$ , which is too large for ICS analysis because it does not sufficiently sample the decay of the beam PSF which acts as the correlator in the measurement. Appropriate pixel sizes for ICS are on the order of  $0.05\text{--}0.1 \mu\text{m}/\text{pixel}$ . **(D)** The interface between the two cells in the region of interest creates a large, bright, heterogeneous signal, which yields an anisotropic correlation function that is fit poorly by Eq. 9. Analyzed areas should be relatively homogeneous with randomly distributed particles. **(E)** Similarly, analyzing a region which includes the edge of a cell introduces a significant artifact in the spatial correlation function **(G)**. Regions analyzed with ICS should be entirely “on cell.” **(F)** An acceptable region for ICS analysis. **(G)** The spatial autocorrelation function for the region outlined in **(E)**. Compare the shape of this function to Fig. 2B

## Applications

Image correlation techniques have been applied to a wide variety of biological systems, using a number of labeling methods and imaging modalities. This section of the review will provide a summary of this body of work. The ICS family of methods is relatively young, and some of the applications to date have been experiments to demonstrate the usefulness or accuracy of a given technique. It is hoped that with time, ICS will be used by more labs, especially in the areas of biology such as cell biology and neuroscience where there is an inherent advantage in observing processes across entire intact cells using imaging.

### Cellular Adhesion and Migration

Cell adhesion and migration are important in a variety of biological processes including embryogenesis, wound healing, and metastasis [90]. Over 50 proteins have been

implicated in adhesion, and their spatiotemporal coordination and localization in adhesion assembly and disassembly has yet to be fully understood [91]. Wiseman et al. [25] used a two-photon LSM and TICS to measure the diffusion of  $\alpha 5$ -integrin-GFP, a membrane protein known to bind to the extracellular matrix (ECM), in the basal membrane of a CHO cell. Two-photon excitation represents a significant advancement for live cell imaging, because the excitation light is less damaging to the cell than the equivalent one-photon wavelength [92]. As well, photobleaching outside the focal plane is reduced compared to single-photon excitation, since it is limited to the focal volume where the laser intensity is high enough to excite fluorophores. In an extension of the earlier work, Wiseman et al. [4] performed an extensive study on the aggregation state and dynamics of  $\alpha 5$ -integrin in living cells. ICS was used to characterize the degree of aggregation of  $\alpha 5$ -integrin, and a calibration with monomeric GFP allowed for a calculation of the absolute number of protein monomers in aggregates. TICS was used to measure the relative diffusing, flowing, and immobile fractions



of GFP constructs of  $\alpha 5$ -integrin and  $\alpha$ -actinin (Fig. 6A). A temporal cross-correlation analysis showed that  $\alpha 5$ -integrin is colocalized with  $\alpha$ -actinin, but not paxillin, throughout the cell outside of adhesions. Finally, STICS was used to map directed fluxes of  $\alpha 5$ -integrin and  $\alpha$ -actinin (Fig. 6B).

The linkage between actin and the ECM plays a central role in regulating cell migration [93]. To understand this interaction, Brown et al. [69] used actin-mRFP constructs in CHO and mouse fibroblast cells also transfected with a GFP construct of  $\alpha$ -actinin,  $\alpha 5$ -integrin, talin, paxillin, vinculin or focal adhesion kinase. By imaging time series of both fluorophores simultaneously, they were able to create velocity maps for both the actin (mRFP) and adhesion related protein (GFP) (Fig. 7). The similarity between the velocity maps for actin and the adhesion proteins was quantified by the relative magnitude of the velocity vectors, as well as their directional correlation [69]. This analysis probed the efficiency of the integrin-actin linkage in different cell types and under different conditions, such as various concentrations of ECM protein on the substrate. They conclude that the linkage is regulated at two levels: one proximal to the  $\alpha$ -actinin in the adhesion, and another proximal to the integrins.

#### Platelet-Derived Growth Factor Receptors

Platelet-derived growth factor (PDGF)  $\beta$ -receptors are implicated in cell growth, chemotaxis, and actin reorganization. It is thought that their oligomerization plays a key role in their activation [94]. In the first application of ICS, Petersen et al. [17] compared the aggregation state of PDGF  $\beta 2$ -receptors before and after the addition of PDGF  $\beta 2$ -receptor antibodies. They quantified the antibody induced clustering of PDGF  $\beta 2$ -receptors using ICS and found that the aggregates after the addition of antibody contained approximately 5 times as many receptors as before. Wiseman et al. [24] later used ICS to find that PDGF- $\beta$  receptors were 3–4 times more clustered at 37°C than at 4°C, and that growth factor PDGF-BB addition did not induce a measurable aggregation at either temperature.

ICS was later optimized to correct for white noise, autofluorescence, and non-specific fluorescence [22]. Using these corrections, Wiseman and Petersen [22] showed using immunolabeling that PDGF  $\beta 2$ -receptors on fixed human fibroblast cells were pre-aggregated at 4 °C. They also estimated these aggregates to be tetramers. A high-order moment analysis of LSM images of PDGF receptors in the same system also found the receptors to be in tetramers after addition of PDGF-BB [32], confirming the findings of the earlier study.

#### Epidermal Growth Factor Receptors

Activation of epidermal growth factor receptors (EGFR) has been shown to trigger cell migration, growth, differentiation, and apoptosis [95]. It is thought that there is a ligand-induced dimerization or oligomerization of receptors at the cell surface, which in turn activates a signaling pathway [96].

Petersen et al. [65] studied antibody-labeled EGFR on A431 cells, which are known to overexpress the receptors (2–3 million per cell). They found a temperature-dependent clustering of EGFR, in which the CD decreased by a factor of 2 while the number of receptors per cluster increased by a factor of 3 as the temperature was decreased from 37 to 4°C.

Clayton et al. [96] used ICS on EGFR-eGFP chimeras in BaF/3 cells to show that EGFR had, on average, 2.2 receptors/cluster in the absence of EGF, and increased to 3.7 receptors/cluster after being exposed to EGF. The cluster density was measured with ICS, and was converted to the number of receptors per cluster by estimating the total number of receptors per cell using comparative flow cytometry. In contrast to the antibody-labeled A431 cells used in [65], the BaF/3 cells expressed EGFR at the normal level of 50,000 copies/cell, and used GFP transfection to label EGFR. Saffarian et al. [97] recently used a modified fluorescence intensity distribution analysis (FIDA) approach to quantify the clustering of EGFR, and found that the values reported by Clayton et al. [96] are likely averages of a heterogeneous distribution of monomers, dimers, and tetramers. Clayton et al. [98] used ICS in conjunction with lifetime-based FRET to measure both sub-micron scale and nanoscale clustering of EGFR in A431 cells.

#### Intracellular Transport

Polyplexes, particles that are comprised of both synthetic polymers and nucleic acids, have recently been proposed as alternatives to viruses for gene delivery [99]. Kulkarni et al. [42] probed the dynamics of endosomes containing fluorescently labeled polyplexes, in living HeLa cells. They used TICS in conjunction with SPT to characterize the motion of an ensemble of polyplexes, and found that their motion was Brownian the majority of the time, with brief periods of directed motion, which they attributed to transport along microtubules.

#### Clathrin-Coated Pits

Clathrin-coated vesicles are the most common route of endocytosis in eukaryotic cells. There is strong evidence



that the AP-2 adapter protein plays a role in binding both clathrin, which forms the lining of the coated pit, and the cargo, which is internalized [100]. Brown and Petersen [101] used ICS to study the distribution of immunofluorescently labeled AP-2 in CV-1 cells, and found that one-third is found in large aggregates associated with clathrin-coated pits, and the remainder is in smaller aggregates with approximately one-third the brightness. Later, a similar system was used to show that ~35% of clathrin was free in the cytosol, while ~65% was in large aggregates in coated pit structures [102]. The same study showed that free clathrin in the cytosol was required for the stability of AP-2 coated pit nucleation sites. CV-1 cells are very appropriate for ICS studies because they are both large and flat [103].

Brown et al. [103] were interested in determining the order of association between clathrin, AP-2, and membrane receptors. Using ICS and ICCS, they found that AP-2 and the membrane receptor were colocalized in cells in which the clathrin lattice was disrupted with treatments. They propose that AP-2 binds membrane proteins prior to associating with clathrin. Later, Boyd et al. [104] used ICS to quantify the clustering and aggregation of AP-2 on different ECM proteins.

Fire et al. [105] found that the degree of clustering in coated pits was directly related to a membrane receptor's affinity for AP-2. This result suggests that the strength of a receptor's internalization signal could strongly influence both its endocytosis rate and lateral mobility.

#### Sendai Virus Fusion

Rasmusson et al. [106] studied the fusion of Sendai virus with living HEp-2 and BALB-3T3 cells. They were able to track the fusion of the viruses by labeling the viral membrane envelope with a fluorescent lipid probe. As the large, bright virus particles bound and then fused to the cell, the fluorescent probe diffused into the plasma membrane. This fusion was measured using ICS, and resulted in an increase in the CD as the lipid probe was dispersed from concentrated viral particles to a diffuse membrane population. Additionally, the effect of incorporating lipophosphoglycan (LPG), a known fusion inhibitor, in the cell membrane was measured quantitatively with ICS.

Rocheleau and Petersen [107] used a fluorescent derivative of the virus receptor GD1a, NBD-GD1a, to study the effect of Sendai virus addition on the aggregation state of the receptor in living CV-1 cells. The cluster density of NBD-GD1a was monitored using ICS, and exhibited a concentration-dependent clustering when virus was added. Furthermore, by labeling the virus with a different emission wavelength fluorophore, DiQ, and using ICCS, it was possible to show that the virus particles bound to the

diffuse population of NBD-GD1a, because there was not a significant cross-correlation between the virus particles and receptor aggregates. Rocheleau and Petersen [108] later fluorescently labeled both the virus protein and lipid components with FITC and DiQ, respectively, and quantitatively followed their dispersion into the cell membrane upon fusion using ICS.

#### Caveolin-1 and Bone Morphogenetic Protein Receptors

Bone morphogenetic proteins (BMPs) have been shown to play key roles in a number of biological processes including embryonic development and postnatal bone formation [109]. Caveolae are membrane systems, often in the form of flask-shaped invaginations, that are involved in endocytosis and signal transduction [110]. Nohe et al. [111] used ICCS in conjunction with dual-color antibody labeling to show that ~25% of caveolin-1, a key protein in the formation of caveolae, is colocalized with BMP receptors type-Ia and -II, as well as EGFR. This was later extended to study the effect of BMP receptor stimulation with BMP-2 on the distribution of caveolin-1 isoforms and BMP receptors [112]. The aggregation of BMP-type-II and -type-Ia receptors and their role in activating the Smad signalling pathway, were also studied using ICS [113].

#### Counting Dendritic Spines

Changes in the number density of dendritic spines on neurons have been implicated as an indicator of synaptic plasticity [114]. Dendritic spines in light microscopy images of neuronal tissue are traditionally manually counted in a time-consuming procedure. Wiseman et al. [29] showed that ICS could yield number densities of spines, which agreed with the manual counting method, had a comparable precision, and could be obtained more quickly. This advance has not yet been adopted by other neuroscience groups probably due to the fact that it was communicated in a technical microscopy journal which would have a restricted readership amongst neuroscientists.

#### Membrane Domains

Bates et al. [115] studied the lateral diffusion of cystic fibrosis transmembrane conductance regulator (CFTR), a transmembrane protein, in living BHK cells using three different techniques: TICS, FRAP, and SPT. CFTR was labeled using streptavidin-Alexa488, -Alexa568, or -QD fluorophores bound to an enzymatically attached biotin

tag on an extracellular loop of the protein. Both FRAP and TICS found that >50% of the protein is immobilized at the cell surface. Interestingly, they found that FRAP consistently measured a higher diffusion coefficient than TICS measurements on the same system. SPT analysis of the QD-labeled protein revealed that a histidine tag mutant CFTR underwent transient confinement in the cell membrane. Computer simulations suggested that this transient confinement could be responsible for the difference in  $D$  measured using TICS and FRAP, since TICS was more sensitive than FRAP to the transiently confined population. Srivastava and Petersen [35] also found a similar difference between TICS and FRAP measurements of the diffusion of antibody-labeled transferrin receptors. They attributed this discrepancy to TICS measuring the diffusion of large aggregates of receptors, and FRAP probing the diffusion of receptor monomers, but the computer simulations do not support this interpretation.

In the first application of PICS, the mobility of a eYFP/H-Ras mutant in live 3T3 cells was measured [87]. The membrane-anchored protein was found to exist in two populations: one which exhibited a fast, free diffusion ( $0.73 \pm 0.01 \mu\text{m}^2/\text{s}$ ), and another which diffused more slowly ( $0.10 \pm 0.01 \mu\text{m}^2/\text{s}$ ), and was found to be confined to domains less than 200 nm in size. In the future, PICS should prove to be a useful alternative to SPT for detecting sub-micron confinement zones.

Putative lipid rafts in biological membranes are cholesterol enriched domains which are thought to play a role in signal transduction [44]. As a model raft protein, Nohe et al. [36] studied a glycosylphosphatidylinositol (GPI) lipid tagged with GFP. They found that the GPI-GFP is distributed in two populations: a homogeneous distribution, which moves too quickly to be measured via TICS, and a population of larger clusters that diffuses at a rate of  $6 \times 10^{-12} \text{ cm}^2/\text{s}$ . They also studied the effect of cholesterol depletion and temperature on the measured diffusion coefficient and cluster density of the slower moving population.

Wang and Axelrod [116] used spatial autocorrelation functions to examine acetylcholine receptors (AChR) on rat myotubes. The size, periodicity, and spatial anisotropy of the AChR clusters were measured from the correlation function. As well, they introduced a novel method to prevent long range (i.e., low spatial frequency) variations in the image from masking short range (i.e., high spatial frequency) fluctuations.

Hwang et al. [117] used near-field scanning optical microscopy (NSOM) to image antibody labeled HLA-I membrane proteins. By calculating circularly averaged spatial autocorrelation functions from images, they were able to measure two distinct domain sizes of protein patches. A similar approach was used to characterize model

membranes containing dipalmitoylphosphatidylcholine (DPPC), dilauroylphosphatidylcholine (DLPC), and cholesterol [118].

### Fluorophore Photophysics

Bachir et al. [119] used TICS to characterize the blinking dynamics of QD ensembles. They immobilized QDs on a glass coverslip, and imaged them using a TIRFM and CCD camera. They found that while temporal correlation functions for single QDs were dominated by long “on” and “off” times (on the order of 100 s), the correlation functions for ensembles of dots were well-fit by a power law:

$$r(\tau) = A - B\tau^\alpha. \quad (30)$$

By changing the excitation laser intensity, the underlying blinking statistics of the QDs were altered, and these changes could be characterized by changes in the  $\alpha$  fitting parameter.

Duriscic et al. [81] used computer simulations and QDs in glycerol to show that TICS decays of samples containing blinking QDs are well fit by models taking only diffusion into account. However, the diffusion coefficient recovered from such analyses is significantly biased to higher diffusion coefficients because of the fluctuations introduced by the fluorophore blinking fluctuations. They showed that a kICS analysis of the same image time series measures the QD mobility independently of photophysics. Finally, they analyzed an image series of a QD-labeled GPI-anchored protein, CD73, in the membrane of fibroblast cells using both TICS and kICS and measured different diffusion coefficients, in agreement with the computer simulations and model system.

The kinetics of GFP photobleaching have been measured using kICS as a proof-of-principle to show that fluorophore photophysics could easily be extracted independently of dynamics from a k-space time correlation function [80]. Although this demonstration measured monoexponential photobleaching, kICS could also be applied to more complex photophysics, such as QD blinking which is governed by a power-law distribution.

### Conclusions

The progeny of ICS discussed in this review comprise a powerful toolbox for studying the dynamics, aggregation state, number density and interactions of membrane and cytosolic fluorescently labeled proteins in living cells. Importantly, they do not require custom made equipment, and can be applied to image series acquired on commercial LSMs and TIRFMs. Although we have presented

a number of varied applications of ICS techniques, their use is still in its infancy. With the further development of both methodology and microscopy, the power of the techniques and the breadth of their applications are bound to grow.

**Acknowledgments** We thank the reviewers for their careful reading of the manuscript, and excellent suggestions. Additionally, DLK thanks the Natural Sciences and Engineering Research Council (NSERC) of Canada for a Canada Graduate Scholarship and PWW acknowledges NSERC and the Canadian Institutes of Health Research.

## References

- Heldin, C.-H. (1995). Dimerization of cell surface receptors in signal transduction. *Cell*, 80, 213–223.
- Lemmon, M. A., & Schlessinger, J. (1994). Regulation of signal transduction and signal diversity by receptor oligomerization. *Trends in Biochemical Sciences*, 19, 459–463.
- Sheets, E. D., Simson, R., & Jacobson, K. (1995). New insights into membrane dynamics from the analysis of cell surface interactions by physical methods. *Current Opinion in Cell Biology*, 7, 707–714.
- Wiseman, P. W., Brown, C. M., Webb, D. J., Hebert, B., Johnson, N. L., Squier, J. A., Ellisman, M. H., & Horwitz, A. F. (2004). Spatial mapping of integrin interactions and dynamics during cell migration by image correlation microscopy. *Journal of Cell Science*, 117, 5521–5534.
- Tserkovnyak, Y., & Nelson, D. R. (2006). Conditions for extreme sensitivity of protein diffusion in membranes to cell environments. *Proceedings of the National Academy of Sciences of the United States of America*, 103, 15002–15007.
- Tsien, R. Y. (1998). The green fluorescent protein. *Annual Review of Biochemistry*, 67, 509–544.
- Magde, D., Elson, E., & Webb, W. W. (1972). Thermodynamic fluctuations in a reacting system—measurement by fluorescence correlation spectroscopy. *Physical Review Letters*, 29, 705–708.
- Elson, E. L., & Magde, D. (1974). Fluorescence correlation spectroscopy. I. Conceptual basis and theory. *Biopolymers*, 13, 1–27.
- Magde, D., Elson, E. L., & Webb, W. W. (1974). Fluorescence correlation spectroscopy. II. An experimental realization. *Biopolymers*, 13, 29–61.
- Magde, D., Webb, W. W., & Elson, E. L. (1978). Fluorescence correlation spectroscopy. III. Uniform translation and laminar flow. *Biopolymers*, 17, 361–376.
- Weissman, M., Schindler, H., & Feher, G. (1976). Determination of molecular weights by fluctuation spectroscopy: Application to DNA. *Proceedings of the National Academy of Sciences of the United States of America*, 73, 2776–2780.
- Petersen, N. O. (1986). Scanning fluorescence correlation spectroscopy. I. Theory and simulation of aggregation measurements. *Biophysical Journal*, 49, 809–815.
- Petersen, N. O., Johnson, D. C., & Schlesinger, M. J. (1986). Scanning fluorescence correlation spectroscopy. II. Application to virus glycoprotein aggregation. *Biophysical Journal*, 49, 817–820.
- St-Pierre, P. R., & Petersen, N. O. (1990). Relative ligand binding to small or large aggregates measured by scanning correlation spectroscopy. *Biophysical Journal*, 58, 503–511.
- Meyer, T., & Schindler, H. (1988). Particle counting by fluorescence correlation spectroscopy. Simultaneous measurement of aggregation and diffusion of molecules in solutions and in membranes. *Biophysical Journal*, 54, 983–993.
- Koppel, D. E., Morgan, F., Cowan, A. E., & Carson, J. H. (1994). Scanning concentration correlation spectroscopy using the confocal laser microscope. *Biophysical Journal*, 66, 502–507.
- Petersen, N. O., Høddelius, P. L., Wiseman, P. W., Seger, O., & Magnusson, K. E. (1993). Quantitation of membrane receptor distributions by image correlation spectroscopy: Concept and application. *Biophysical Journal*, 65, 1135–1146.
- Berland, K. M., So, P. T., Chen, Y., Mantulin, W. W., & Gratton, E. (1996). Scanning two-photon fluctuation correlation spectroscopy: Particle counting measurements for detection of molecular aggregation. *Biophysical Journal*, 71, 410–420.
- Fink, M. C., Adair, K. V., Guenza, M. G., & Marcus, A. H. (2006). Translational diffusion of fluorescent proteins by molecular Fourier imaging correlation spectroscopy. *Biophysical Journal*, 91, 3482–3498.
- Hebert, B., Costantino, S., & Wiseman, P. W. (2005). Spatio-temporal image correlation spectroscopy (STICS) theory, verification, and application to protein velocity mapping in living CHO cells. *Biophysical Journal*, 88, 3601–3614.
- Cannell, M. B., McMorland, A., & Soeller, C. (2006). Image enhancement by deconvolution. In J. B. Pawley (Ed.), *Handbook of biological confocal microscopy* (pp. 488–500). New York: Springer.
- Wiseman, P. W., & Petersen, N. O. (1999). Image correlation spectroscopy. II. Optimization for ultrasensitive detection of preexisting platelet-derived growth factor-beta receptor oligomers on intact cells. *Biophysical Journal*, 76, 963–77.
- Costantino, S., Comeau, J. W. D., Kolin, D. L., & Wiseman, P. W. (2005). Accuracy and dynamic range of spatial image correlation and cross-correlation spectroscopy. *Biophysical Journal*, 89, 1251–1260.
- Wiseman, P. W., Høddelius, P., Petersen, N. O., & Magnusson, K. (1997). Aggregation of PDGF- $\beta$  receptors in human skin fibroblasts: Characterization by image correlation spectroscopy (ICS). *FEBS Letters*, 401, 43–48.
- Wiseman, P. W., Squier, J. A., Ellisman, M. H., & Wilson, K. R. (2000). Two-photon image correlation spectroscopy and image cross-correlation spectroscopy. *Journal of Microscopy*, 200, 14–25.
- Yoo, H., Song, I., & Gweon, D.-G. (2006). Measurement and restoration of the point spread function of fluorescence confocal microscopy. *Journal of Microscopy*, 221, 172–176.
- Huang, Z., & Thompson, N. L. (1996). Imaging fluorescence correlation spectroscopy: Nonuniform IgE distributions on planar membranes. *Biophysical Journal*, 70, 2001–2007.
- Rocheleau, J. V., Wiseman, P. W., & Petersen, N. O. (2003). Isolation of bright aggregate fluctuations in a multipopulation image correlation spectroscopy system using intensity subtraction. *Biophysical Journal*, 84, 4011–22.
- Wiseman, P. W., Capani, F., Squier, J. A., & Martone, M. E. (2002). Counting dendritic spines in brain tissue slices by image correlation spectroscopy analysis. *Journal of Microscopy*, 205, 177–86.
- Palmer, A. G., & Thompson, N. L. (1989). High-order fluorescence fluctuation analysis of model protein clusters. *Proceedings of the National Academy of Sciences of the United States of America*, 86, 6148–6152.
- Vanden Broek, W., Huang, Z., & Thompson, N. L. (1999). High-order autocorrelation with imaging fluorescence correlation spectroscopy: Application to IgE on supported planar membranes. *Journal of Fluorescence*, 9, 313–324.

32. Sergeev, M., Costantino, S., & Wiseman, P. W. (2006). Measurement of monomer–oligomer distributions via fluorescence moment image analysis. *Biophysical Journal*, 91, 3884–3896.
33. Benn, A. G., & Kulperger, R. J. (1997). Integrated marked poisson processes with application to image correlation spectroscopy. *The Canadian Journal of Statistics*, 25, 215–231.
34. Srivastava, M., & Petersen, N. O. (1996). Image cross-correlation spectroscopy: A new experimental biophysical approach to measurement of slow diffusion of fluorescent molecules. *Methods in Cell Science*, 18, 47–54.
35. Srivastava, M., & Petersen, N. O. (1998). Diffusion of transferrin receptor clusters. *Biophysical Chemistry*, 75, 201–211.
36. Nohe, A., Keating, E., Fivaz, M., van der Goot, F. G., & Petersen, N. O. (2006). Dynamics of GPI-anchored proteins on the surface of living cells. *Nanomedicine* 39, 159–169.
37. Petersen, N. (2001). FCS and spatial correlations on biological surfaces. In R. Rigler & E. S. Elson (Eds.), *Fluorescence correlation spectroscopy* (pp. 162–184). Heidelberg: Springer.
38. Ulrich, M., Wohland, T., Rigler, R., & Vogel, H. (1999). Resolution of fluorescence correlation measurements. *Biophysical Journal*, 76, 1619–1631.
39. Feder, T. J., Brust-Mascher, I., Slattery, J. P., Baird, B., & Webb, W. W. (1996). Constrained diffusion or immobile fraction on cell surfaces: A new interpretation. *Biophysical Journal*, 70, 2767–2773.
40. Aragón, S. R., & Pecora, R. (1976). Fluorescence correlation spectroscopy as a probe of molecular dynamics. *The Journal of Chemical Physics*, 64, 1791–1803.
41. Saxton, M. J., & Jacobson, K. (1997). Single-particle tracking: Applications to membrane dynamics. *Annual Review of Biophysics and Biomolecular Structure*, 26, 373–399.
42. Kulkarni, R. P., Wu, D. D., Davis, M. E., & Fraser, S. E. (2005). Quantitating intracellular transport of polyplexes by spatio-temporal image correlation spectroscopy. *Proceedings of the National Academy of Sciences of the United States of America*, 102, 7523–7528.
43. Kolin, D. L., Costantino, S., & Wiseman, P. W. (2006). Sampling effects, noise, and photobleaching in temporal image correlation spectroscopy. *Biophysical Journal*, 90, 628–639.
44. Lagerholm, B. C., Weinreb, G. E., Jacobson, K., & Thompson, N. L. (2005). Detecting microdomains in intact cell membranes. *Annual Review of Physical Chemistry*, 56, 309–336.
45. Axelrod, D., Koppel, D. E., Schlessinger, J., Elson, E., & Webb, W. W. (1976). Mobility measurement by analysis of fluorescence photobleaching recovery kinetics. *Biophysical Journal*, 16, 1055–1069.
46. Jacobson, K., O'Dell, D., & August, J. T. (1984). Lateral diffusion of an 80,000–dalton glycoprotein in the plasma membrane of murine fibroblasts: Relationships to cell structure and function. *The Journal of Cell Biology*, 99, 1624–1633.
47. Sheetz, M. P., & Koppel, D. E. (1979). Membrane damage caused by irradiation of fluorescent concanavalin. *Proceedings of the National Academy of Sciences of the United States of America*, 76, 3314–3317.
48. Lepock, J. R., Campbell, S. D., Gruber, M., & Kruuv, J. (1979). Photoinduced cell killing and crosslinking of fluorescein conjugated concanavalin A to cell surface proteins. *Biochemical and Biophysical Research Communications*, 91, 1157–1165.
49. Jacobson, K., Hou, Y., & Wojcieszyn, J. (1979). Evidence for lack of damage during photobleaching measurements of the lateral mobility of cell surface components. *Experimental Cell Research*, 116, 179–189.
50. Wolf, D. E., Edidin, M., & Dragsten, P. R. (1980). Effect of bleaching light on measurements of lateral diffusion in cell membranes by the fluorescence photobleaching recovery method. *Proceedings of the National Academy of Sciences of the United States of America*, 77, 2043–2045.
51. Schwille, P., Korch, J., & Webb, W. W. (1999). Fluorescence correlation spectroscopy with single-molecule sensitivity on cell and model membranes. *Cytometry*, 36, 176–182.
52. Nicolau, J., Dan V., Hancock, J. F., & Burrage, K. (2007). Sources of anomalous diffusion on cell membranes: A Monte Carlo study. *Biophysical Journal*, 92, 1975–1987.
53. Manders, E. M. M., Verbeek, F. J., & Aten, J. A. (1993). Measurement of colocalization of objects in dual-color confocal images. *Journal of Microscopy*, 169, 375–382.
54. Costes, S. V., Daelemans, D., Cho, E. H., Dobbin, Z., Pavlakis, G., & Lockett, S. (2004). Automatic and quantitative measurement of protein–protein colocalization in live cells. *Biophysical Journal*, 86, 3993–4003.
55. Comeau, J., Costantino, S., & Wiseman, P. W. (2006). A guide to accurate colocalization measurements. *Biophysical Journal*, 91, 4611–4622.
56. Manders, E. M. M. (1997). Chromatic shift in multicolour confocal microscopy. *Journal of Microscopy*, 185, 321–328.
57. McAuliffe, M. J., Lalonde, F. M., McGarry, D., Gandler, W., Csaky, K., & Trus, B. L. (2001). Medical image processing, analysis & visualization in clinical research in 14th IEEE symposium on computer-based medical systems IEEE computer society (p. 0381).
58. Schwille, P. (2001). Cross-correlation analysis. In R. Rigler & E. S. Elson (Eds.), *FCS in fluorescence correlation spectroscopy: Theory and applications*. New York: Springer. Volume 65 of *Chemical Physics*.
59. Sekar, R. B., & Periasamy, A. (2003). Fluorescence resonance energy transfer (FRET) microscopy imaging of live cell protein localizations. *The Journal of Cell Biology*, 160, 629–633.
60. Milon, S., Hovius, R., Vogel, H., & Wohland, T. (2003). Factors influencing fluorescence correlation spectroscopy measurements on membranes: Simulations and experiments. *Chemical Physics*, 288, 171–186.
61. Stauffer, T. P., & Meyer, T. (1997). Compartmentalized IgE receptor-mediated signal transduction in living cells. *The Journal of Cell Biology*, 139, 1447–1454.
62. Sheets, E. D., Holowka, D., & Baird, B. (1999). Critical role for cholesterol in Lyn-mediated tyrosine phosphorylation of Fc  $\epsilon$  RI and their association with detergent-resistant membranes. *The Journal of Cell Biology*, 145, 877–887.
63. Pyenta, P. S., Holowka, D., & Baird, B. (2001). Cross-correlation analysis of inner-leaflet-anchored green fluorescent protein co-redistributed with IgE receptors and outer leaflet lipid raft components. *Biophysical Journal*, 80, 2120–2132.
64. Hebert, B., Hulme, S. E., & Wiseman, P. W. (2005). Membrane protein dynamics measured by two-photon ring correlation spectroscopy: Theory and application to living cells in multi-photon microscopy in the biomedical sciences V. In A. Periasamy & P. T. So (Eds.) *Proceedings of S.P.I.E.* (Vol. 5700, pp. 109–117).
65. Petersen, N. O., Brown, C., Kaminski, A., Rocheleau, J., Srivastava, M., & Wiseman, P. W. (1998). Analysis of membrane protein cluster densities and sizes in situ by image correlation spectroscopy. *Faraday Discuss* (pp. 289–305); discussion 331–343.
66. Ji, L., & Danuser, G. (2005). Tracking quasi-stationary flow of weak fluorescent signals by adaptive multi-frame correlation. *Journal of Microscopy*, 220, 150–167.
67. Adrian, R. J. (2005). Twenty years of particle image velocimetry. *Experiments in Fluids*, 39, 159–169.
68. Gui, L., & Merzkirch, W. (2000). A comparative study of the MQD method and several correlation-based PIV evaluation algorithms. *Experiments in Fluids*, 28, 36–44.

69. Brown, C. M., Hebert, B., Kolin, D. L., Zareno, J., Whitmore, L., Horwitz, A. F., & Wiseman, P. W. (2006). Probing the Integrin-Actin Linkage using High Resolution Protein Velocity Mapping. *Journal of Cell Science*, 119, 5204–5214.
70. Hebert, B. (2006). Spatio-temporal image correlation spectroscopy: Development and implementation in living cells Ph.D. thesis McGill University.
71. Sinnecker, D., Voigt, P., Hellwig, N., & Schaefer, M. (2005). Reversible photobleaching of enhanced green fluorescent proteins. *Biochemistry*, 44, 7085–7094.
72. Dickson, R. M., Cubitt, A. B., Tsien, R. Y., & Moerner, W. E. (1997). On/Off blinking and switching behaviour of single molecules of green fluorescent protein. *Nature*, 388, 355–358.
73. Doose, S., Tsay, J. M., Pinaud, F., & Weiss, S. (2005). Comparison of photophysical and colloidal properties of biocompatible semiconductor nanocrystals using fluorescence correlation spectroscopy. *Analytical Chemistry*, 77, 2235–2242.
74. Bruchez, M., Moronne, M., Gin, P., Weiss, S., & Alivisatos, A. P. (1998). Semiconductor nanocrystals as fluorescent biological labels. *Science*, 281, 2013–2016.
75. Chan, W. C. W., & Nie, S. (1998). Quantum dot bioconjugates for ultrasensitive nonisotopic. *Detection Science*, 281, 2016–2018.
76. Yao, J., Larson, D. R., Vishwasrao, H. D., Zipfel, W. R., & Webb, W. W. (2005). Blinking and nonradiant dark fraction of water-soluble quantum dots in aqueous solution. *Proceedings of the National Academy of Sciences of the United States of America*, 102, 14284–14289.
77. Kuno, M., Fromm, D. P., Hamann, H. F., Gallagher, A., & Nesbitt, D. J. (2000). Nonexponential “blinking” kinetics of single CdSe quantum dots: A universal power law behavior. *The Journal of Chemical Physics*, 112, 3117–3120.
78. Margolin, G., & Barkai, E. (2004). Aging correlation functions for blinking nanocrystals, and other on–off stochastic processes. *The Journal of Chemical Physics*, 121, 1566–1577.
79. Margolin, G., & Barkai, E. (2005). Nonergodicity of blinking nanocrystals and other Lévy-walk processes. *Physical Review Letters*, 94, 080601.
80. Kolin, D. L., Ronis, D., & Wiseman, P. W. (2006). k-Space image correlation spectroscopy: A method for accurate transport measurements independent of fluorophore photophysics. *Biophysical Journal*, 91, 3061–3075.
81. Durisic, N., Bachir, A. I., Kolin, D. L., Hebert, B., Lagerholm, B. C., Grutter, P., & Wiseman, P. W. (2007). Detection and correction of blinking bias in image correlation transport measurements of quantum dot tagged macromolecules. *Biophysical Journal*, 93, 1338–1346.
82. Berne, B. J., & Pecora, R. (2000). Dynamic light scattering. New York: Dover.
83. Hattori, M., Shimizu, H., & Yokoyama, H. (1996). Fluorescence correlation spectroscopy with traveling interference fringe excitation. *The Review of Scientific Instruments*, 67, 4064–4071.
84. Digman, M. A., Sengupta, P., Wiseman, P. W., Brown, C. M., Horwitz, A. R., & Gratton, E. (2005). Fluctuation correlation spectroscopy with a laser-scanning microscope: Exploiting the hidden time structure. *Biophysical Journal*, 88, L33–L36.
85. Digman, M. A., Brown, C. M., Sengupta, P., Wiseman, P. W., Horwitz, A. R., & Gratton, E. (2005). Measuring fast dynamics in solutions and cells with a laser scanning microscope. *Biophysical Journal*, 89, 1317–1327.
86. Thompson, N. L. (1991). Fluorescence correlation spectroscopy in topics. In J. R. Lakowicz (Ed.), *Fluorescence spectroscopy, volume 1: Techniques* (pp. 337–378). New York: Plenum Press.
87. Semrau, S., & Schmidt, T. (2007). Particle image correlation spectroscopy (PICS): Retrieving nanometer-scale correlations from high-density single-molecule position data. *Biophysical Journal*, 92, 613–621.
88. Brown, C. M. (2007). Fluorescence microscopy—avoiding the pitfalls. *Journal of Cell Science*, 120, 1703–1705.
89. Hibbs, A. R., MacDonald, G., & Garsha, K. (2006). Practical confocal microscopy. In J. B. Pawley (Ed.), *Handbook of biological confocal microscopy* (pp. 650–671). New York: Springer.
90. Lauffenburger, D. A., & Horwitz, A. F. (1996). Cell migration: A physically integrated molecular process. *Cell*, 84, 359–369.
91. Webb, D. J., Parsons, J. T., & Horwitz, A. F. (2002). Adhesion assembly, disassembly and turnover in migrating cells—over and over and over again. *Nature Cell Biology*, 4, E97–E100.
92. Denk, W., Strickler, J. H., & Webb, W. W. (1990). Two-photon laser scanning fluorescence microscopy. *Science*, 248, 73–76.
93. Ridley, A. J., Schwartz, M. A., Burridge, K., Firtel, R. A., Ginsberg, M. H., Borisy, G., Parsons, J. T., & Horwitz, A. R. (2003). Cell migration: Integrating signals from front to back. *Science*, 302, 1704–1709.
94. Heldin, C.-H., Östman, A., & Rönstrand, L. (1998). Signal transduction via platelet-derived growth factor receptors. *Biochimica et Biophysica Acta*, 1378, F79–F113.
95. Yarden, Y., & Slivkowski, M. X. (2001). Untangling the ErbB signalling network. *Nature Reviews. Molecular Cell Biology*, 2, 127–137.
96. Clayton, A. H. A., Walker, F., Orchard, S. G., Henderson, C., Fuchs, D., Rothacker, J., Nice, E. C., & Burgess, A. W. (2005). Ligand-induced dimer-tetramer transition during the activation of the cell surface epidermal growth factor receptor—A multi-dimensional microscopy analysis. *The Journal of Biological Chemistry*, 280, 30392–30399.
97. Saffarian, S., Li, Y., Elson, E. L., & Pike, L. J. (2007). Oligomerization of the EGF receptor investigated by live cell fluorescence intensity distribution analysis. *Biophysical Journal*, 93, 1021–1031.
98. Clayton, A. H. A., Tavarnesi, M. L., & Johns, T. G. (2007). Unligated epidermal growth factor receptor forms higher order oligomers within microclusters on A431 cells that are sensitive to tyrosine kinase inhibitor binding. *Biochemistry*, 46, 4589–4597.
99. Haag, R., & Kratz, F. (2006). Polymer therapeutics: Concepts and applications. *Angewandte Chemie (International edition in English)*, 45, 1198–1215.
100. Traub, L. M. (2003). Sorting it out: AP-2 and alternate clathrin adaptors in endocytic cargo selection. *The Journal of Cell Biology*, 163, 203–208.
101. Brown, C. M., & Petersen, N. O. (1998). An image correlation analysis of the distribution of clathrin associated adaptor protein (AP-2) at the plasma membrane. *Journal of Cell Science*, 111(Pt 2), 271–281.
102. Brown, C. M., & Petersen, N. O. (1999). Free clathrin triskelions are required for the stability of clathrin-associated adaptor protein (AP-2) coated pit nucleation sites. *Biochem. Cell Biol.*, 77, 439–448.
103. Brown, C. M., Roth, M. G., Henis, Y. I., & Petersen, N. O. (1999). An internalization-competent influenza hemagglutinin mutant causes the redistribution of AP-2 to existing coated pits and is colocalized with AP-2 in clathrin free clusters. *Biochemistry*, 38, 15166–15173.
104. Boyd, N. D., Chan, B. M. C., & Petersen, N. O. (2002). Adaptor protein-2 exhibits  $\alpha_1\beta_1$  or  $\alpha_6\beta_1$  integrin-dependent redistribution in rhabdomyosarcoma cells. *Biochemistry*, 41, 7232–7240.
105. Fire, E., Brown, C. M., Roth, M. G., Henis, Y. I., & Petersen, N. O. (1997). Partitioning of proteins into plasma membrane microdomains. Clustering of mutant influenza virus



- hemagglutinins into coated pits depends on the strength of the internalization signal. *The Journal of Biological Chemistry*, 272, 29538–29545.
106. Rasmusson, B. J., Flanagan, T. D., Turco, S. J., Epand, R. M., & Petersen, N. O. (1998). Fusion of Sendai virus and individual host cells and inhibition of fusion by lipophosphoglycan measured with image correlation spectroscopy. *Biophysica et Biophysica Acta*, 1404, 338–352.
  107. Rocheleau, J. V., & Petersen, N. O. (2000). Sendai virus binds to a dispersed population of NBD-GD1a. *Bioscience Reports*, 20, 139–155.
  108. Rocheleau, J. V., & Petersen, N. O. (2001). The Sendai virus membrane fusion mechanism studied using image correlation spectroscopy. *European Journal of Biochemistry*, 268, 2924–2930.
  109. Chen, D., Zhao, M., & Mundy, G. R. (2004). Bone morphogenetic proteins. *Growth Factors*, 22, 233–241.
  110. Anderson, R. G. W. (1998). The caveolae membrane system. *Annual Review of Biochemistry*, 67, 199–225.
  111. Nohe, A., Keating, E., Loh, C., Underhill, M. T., & Petersen, N. O. (2004a). Caveolin-1 isoform reorganization studied by image correlation spectroscopy. *Faraday Discuss*, 126, 185–195.
  112. Nohe, A., Keating, E., Underhill, M. T., Knaus, P., & Petersen, N. O. (2004b). Dynamics and interaction of caveolin-1 isoforms with BMP-receptors. *Journal of Cell Science*, 118, 643–650.
  113. Nohe, A., Keating, E., Underhill, T. M., Knaus, P., & Petersen, N. O. (2003). Effect of the distribution and clustering of the type I A BMP receptor (ALK3) with the type II BMP receptor on the activation of signalling pathways. *Journal of Cell Science*, 116, 3277–3284.
  114. Moser, M. B., Trommald, M., & Andersen, P. (1994). An increase in dendritic spine density on hippocampal CA1 pyramidal cells following spatial learning in adult rats suggests the formation of new synapses. *Proceedings of the National Academy of Sciences of the United States of America*, 91, 12673–12675.
  115. Bates, I. R., Hebert, B., Luo, Y., Liao, J., Bashir, A. I., Kolin, D. L., Wiseman, P. W., & Hanrahan, J. W. (2006). Membrane lateral diffusion and capture of CFTR within transient confinement zones. *Biophysical Journal*, 91, 1046–1058.
  116. Wang, M. D., & Axelrod, D. (1994). Microclustering patterns of acetylcholine receptors on myotubes studied by spatial fluorescence autocorrelation. *Bioimaging*, 2, 22–35.
  117. Hwang, J., Gheber, L. A., Margolis, L., & Edidin, M. (1998). Domains in cell plasma membranes investigated by near-field scanning optical microscopy. *Biophysical Journal*, 74, 2184–2190.
  118. Tokumasu, F., Hwang, J., & Dvorak, J. A. (2004). Heterogeneous molecular distribution in supported multicomponent lipid bilayers. *Langmuir*, 20, 614–618.
  119. Bachir, A. I., Durisic, N., Hebert, B., Grütter, P. H., & Wiseman, P. W. (2006). Image correlation spectroscopy studies of blinking dynamics in semiconductor quantum dots. *Journal of Applied Physics*, 99, 064503.